Bidirectional differentiation of BMSCs induced by a biomimetic procallus based on a gelatin-reduced graphene oxide reinforced hydrogel for rapid bone regeneration

Delong Jiao [a,1], Ao Zheng [a,1], Yang Liu [b], Xiangkai Zhang [a], Xiao Wang [a], Jiannan Wu [a], Wenjun She [a], Kaige Lv [a], Lingyan Cao [a,*], Xinquan Jiang [a,**]

[a] *Department of Prosthodontics, Shanghai Engineering Research Center of Advanced Dental Technology and Materials, Shanghai Key Laboratory of Stomatology & Shanghai Research Institute of Stomatology, National Clinical Research Center for Oral Diseases, Shanghai Ninth People's Hospital, College of Stomatology, Shanghai Jiao Tong University School of Medicine, China*
[b] *The State Key Laboratory of Bioreactor Engineering, East China University of Science and Technology, 130 Meilong Road, Shanghai 200237, China*

A B S T R A C T

Developmental engineering strategy needs the biomimetic composites that can integrate the progenitor cells, biomaterial matrices and bioactive signals to mimic the natural bone healing process for faster healing and reconstruction of segmental bone defects. We prepared the gelatin-reduced graphene oxide (GOG) and constructed the composites that mimicked the procallus by combining the GOG with the photo-crosslinked gelatin hydrogel. The biological effects of the GOG-reinforced composites could induce the bi-differentiation of bone marrow stromal cells (BMSCs) for rapid bone repair. The proper ratio of GOG in the composites regulated the composites' mechanical properties to a suitable range for the adhesion and proliferation of BMSCs. Besides, the GOG-mediated bidirectional differentiation of BMSCs, including osteogenesis and angiogenesis, could be activated through Erk1/2 and AKT pathway. The methyl vanillate (MV) delivered by GOG also contributed to the bioactive signals of the biomimetic procallus through priming the osteogenesis of BMSCs. During the repair of the calvarial defect *in vivo*, the initial hypoxic condition due to GOG in the composites gradually transformed into a well-vasculature robust situation with the bi-differentiation of BMSCs, which mimicked the process of bone healing resulting in the rapid bone regeneration. As an inorganic constituent, GOG reinforced the organic photo-crosslinked gelatin hydrogel to form a double-phase biomimetic procallus, which provided the porous extracellular matrix microenvironment and bioactive signals for the bi-directional differentiation of BMSCs. These show a promised application of the bio-reduced graphene oxide in biomedicine with a developmental engineering strategy.

1. Introduction

As one of the three elements of tissue engineering [1], scaffold plays a role in loading cells and protein factors. The ideal scaffold material may integrate protein factors and cells to construct a biomimetic structural environment to simulate the physiologic repair process for efficient and high-quality reconstruction. Lenas et al. first proposed the concept of developmental tissue engineering in his two reviews in 2009 [2,3], the core of which is simulating the physiological development process. Similarly, bone healing and bone development involve complex and autonomous courses such as intramembranous, osteogenesis, and endochondral osteogenesis [4,5], which have the following three characteristics. (1) Path-dependence: subsequent developments depend on the physiological conditions provided by the antecedent physiological process. (2) Robustness: self-physiological process can resist the influence of external adverse factors. (3) Semi-autonomy: a certain degree of autonomous regulation and development ability (Fig. 1a). The bone fracture healing process (Fig. 1a) includes three consecutive phases:

Fig. 1. The developmental engineering strategy for the biomimetic procallus. a) Schematic illustration of the bone healing process and the path-dependent, robust, and semi-autonomous nature of the developmental engineering strategy. b) Schematic diagram of the biomimetic procallus with the realm of developmental engineering.

inflammatory, reparative, and remodeling [6]. Complex spatial and temporal distribution of cells occurs at each phase and interacts with the extracellular matrix (ECM) to construct a bioactive signal microenvironment for the fracture healing [7]. Initially, a coagulation cascade forms the hematoma along with the infiltration of progenitor cells in the trauma. The hypoxic microenvironment due to the disrupted vasculature in hematoma leads to the differentiation of the progenitor cells recruited from the exposed periosteum and bone marrow. The bioactive signals that were established by the survived stem cells in the initial inflammatory phase activate the subsequent progenitor aggregation and intermediate fibrous tissue (procallus) formation for intramembranous (IM) and endochondral (EC) ossification. At the early reparative phase, a spanning procallus takes up most fracture space and serves a primed template for subsequent reparative and remodeling phases. The elaborate constructions of progenitor cells, ECM microenvironment, and bioactive signals in procallus present a promised bio-inspired synthesis strategy for improving bone regeneration, which implies that the procallus acts as a pivotal role in the developmental engineering strategy. At last, we hypothesize that the biomimetic procallus with the path-dependent, robust, and semi-autonomous nature of the developmental engineering, promises a potentially extensive and efficient bone regeneration.

The two-dimensional nanomaterial, graphene oxide (GO), has been used as a reinforcement agent to improve the physical properties of composites for tissue engineering applications [8–11] due to its unique features, such as excellent tensile modulus (1.0 TPa), ultimate strength

(130 GPa), distinctive electrical and thermal properties [12]. Moreover, GO can be used as drug deliver due to its large specific surface area for drug loading through forming strong π-π conjugation with the drug molecules [13]. It was also reported that GO could be taken up by cells through endocytosis [14]. Furthermore, graphene and graphene-based materials promoted osteogenic differentiation of mesenchymal stem cells [15–17] and angiogenesis *in vitro* by activation of phospho-eNOS [18]. However, GO was reported with poor solubility and stability in physiological environments and its application is partially limited [19]. Compared with GO, the reduced GO was more suitable for biomedical applications, such as drug and gene delivery, antibacterial agents, biosensing, bioimaging, and tissue engineering, which can be ascribed to the modification from reduction [20–22].

Recently, hydrogel has been applied in various areas of biomedical engineering [23], such as substitutes for cartilage and skin, wound dressing and scaffolds for bone tissue engineering [24], since they can mimic the ECM due to their highly swollen 3D environment with a high water content and its tissue-like elastic properties [25]. Nowadays, different natural materials have been utilized to generate the hydrogels, among which gelatin is a natural material and the major component of skin, bone, cartilage, and connective tissues. Due to its availability, biocompatibility and biodegradability, gelatin has been extensively applied in the tissue engineering [26]. Meanwhile, gelatin is known not only for biocompatible hydrogel, but also as a biocompatible polypeptide with obvious reducibility due to abundant amino side chain on its backbone of molecular chain [27]. It's reported that the

photo-crosslinked rapid prototyping method using ruthenium-based photochemistry was a simple, stable, and quick method to prepare gelatin hydrogels [28–32]. The ruthenium-based photochemistry could form a stable gelatin hydrogel by producing tyrosine involved covalent bond crosslinks in gelatin hydrogel. Due to the interactions between the tyrosines on the surface of the gelatin chain, the photo-crosslinked gelatin hydrogel's overall mechanical properties could be improved by inhibiting the formation of triple helices in gelatin [33]. Gelatin has reducibility and has been used in the development industry [34,35]. In our previous study [36], we prepared reduced-GO from gelatin (gelatin-reduced graphene oxide, GOG), we combined GOG and gelatin to construct the reinforced composite to mimic the procallus through the tyrosine involved covalent bond interlace for developmental engineering application. We also found that the GOG could synergistically promote the osteogenesis with a Wnt/β-catenin agonist, methyl vanillate (MV) [36]. Thus, we selected MV as the primed bioactive factor delivered by GOG for further promoting the osteogenic effect of the biomimetic procallus. These properties of GOG make it act as a pivotal factor in mimicking the intricate pattern of ECM microenvironment and bioactive signals in the procallus for supporting the differentiation of progenitor cells. The biomimetic procallus may provide a bio-inspired synthesized template for the progenitor cell differentiation and rapid repair of the bone defect with the realm of developmental engineering strategy (Fig. 1b).

In this study, GOG was creatively used to construct the bionic procallus, and its application in bone repair and regeneration was investigated. On the one hand, the mechanical properties of biomimetic hydrogels can be improved by using GOG as a nano reinforcing agent through the reaction of the covalent bond of tyrosine with gelatin. On the other hand, GOG could also be used as a controlled release carrier of MV to change the anoxic microenvironment of the composite materials which could regulate osteogenic and angiogenesis in BMSCs, so as to achieve rapid bone regeneration. In this study, the endocytosis mechanism and intracellular localization of GOG in bone marrow stromal cells (BMSCs) were studied. We also used MV loaded GOG combined with photo-linked gelatin hydrogel to investigate its ability to regulate BMSCs differentiation and the corresponding mechanism. In addition, BMSCs loaded biomimetic hydrogels were used to study the effect of rapid bone repair *in vivo*. Generally, a new type of procallus was prepared combined MV loaded GOG with photo-crosslinking gelatin gel system, which provide a new tissue engineering strategy for rapid bone repair and regeneration.

2. Experimental section

2.1. Isolation and culture of bone marrow mesenchymal stem cells (BMSCs)

This process was conducted as a previous description [37]. Primary BMSCs were collected from Sprague-Dawley rats (Shanghai SLAC Laboratory, Shanghai, China). Bone marrow was firstly washed with Dulbecco's modified Eagle medium (DMEM; HyClone, USA) supplemented with 1% penicillin/streptomycin (HyClone, USA). Then through centrifugation, we collected the cell pellet without blood cells and mixed it with complete DMEM (FBS; Gibco, USA) supplemented with 10% fetal bovine serum. The mixtures were plated into culture flasks to get the cell colonies. Then the cells were passaged by trypsinization after convergence formation. Besides, we experimented with BMSCs obtained from 2 to 3 generations.

2.2. Preparation and physical characterization of GOG

GOG was prepared through reducing GO with gelatin as a previous description [36] and stored in water with 1.0 mg/mL concentration at 4 °C for further use (Figure S1, Supporting information). Here are brief descriptions of the synthesis process, firstly 50 mL of 0.2 mg/mL GO

aqueous dispersion was prepared and then added dropwise into 50 mL of homogeneous gelatin solution under stirring at 80 °C for 1 h. The mixture would react at 95 °C under stirring for 24 h, then the acquired stable black dispersion liquid was centrifuged at 20,000 rpm and washed with hot water three times to remove the excess gelatin after reaction. At last, the obtained GOG after remove of excess gelatin was resuspended in water and stored at 4 °C until use. For investigation on the difference of the solubilities between GO and GOG, we suspended them in phosphate buffer saline (PBS), alcohol, DMEM, and simulated body fluid (SBF) by ultrasonic and observed the sedimentation of them in various solvents at 2 h and 4 h. Nicomp 380 particle sizer (Z3000, PSS, USA) was used to test the particle size and zeta potential of GO and GOG. The morphology of the GOG was studied usingSCANIs scanning electron microscope (SEM) and transmission electron microscope (TEM) as a previous description [36]. X-ray diffraction (XRD) and FTIR spectrum were also conducted to verify the successful reduction of GO and investigate the difference between them by the methods described in our previous research [36]. Tyrosine content of GO and GOG was tested using Tyrosine Colorimetric Assay Kit (MAK219, Sigma, USA) through measuring a colorimetric product with absorbance at 492 nm, and the results were expressed as the mass ratio of tyrosine to the total weight.

2.3. Distribution and endocytosis mechanism of GOG in BMSCs

The cellular uptake of GOG by BMSCs after co-culture for 2 h was investigated by the TEM. The ultra-thin sections (70 nm) were prepared by Leica EM UC7 ultramicrotome and taken photos by TEM (H-7650; Hitachi, Tokyo, Japan) to visualize the uptake of GOG by BMSCs. Rhodamine 6G (R6G) labeled GOG was prepared as a previous description [36], and then BMSCs were incubated with R6G labeled GOG for 2 h. After the endocytosis of GOG by BMSCs, the cells were fixed using 4% phosphate paraformaldehyde and stained with FITC-labeled phalloidin and DAPI before recording by CLSM (LEICA, Germany). To explore the endocytosis mechanisms of GOG in BMSCs in-depth insight, a series of assays were conducted to illustrate GOG's track. The BMSCs were pretreated with the medium containing different inhibitors for 2 h incubation before the endocytosis of GOG. The affected mechanisms of the inhibitors and suitable concentrations for exerting pharmacodynamics were described in the previous studies reported by other researchers [38–42]. After 2 h of co-incubation with the inhibitors and R6G labeled GOG, the BMSCs were analyzed using CLSM (LEICA, Germany) to see the change of GOG uptake. Meanwhile, flow cytometry analysis was performed on the MoFlo XDP flow cytometry system (BECKMAN COULTER, USA) to quantify the differences. To observe the influence of mitosis and autophagy on the endocytosis of GOG, the tubulin or LC3B was incubated with primary antibody (ab52866 or ab192890; Abcam, USA) overnight at 4 °C and then stained with the goat anti-rabbit Alexa Fluor® 647 (Abcam, USA) the second antibody in the colchicine treated group (pretreated with colchicine for 2 h and 24 h) or the wortmannin/amiloride treated group respectively. The β-actin and nuclei were stained as described above, and the images were captured by CLSM (LEICA, Germany).

2.4. Preparation and physical characterization of the PH/GOG composites

We prepared the crosslinked composites using the principle of photochemical reaction [28], in which the 50 mM [RuII(bpy)$_3$]$^{2+}$ and 1 M sodium persulphate (SPS) aqueous solutions as the stock solutions were applied to initiate the reactions. Various amounts of GOG (0, 5, 10, 15, 20, 30, 40 or 50 μL of 35 mg/mL GOG in PBS, pH 7.4), were mixed in the 1 mL 100 mg/mL gelatin/PBS solution with addition of 20 μL [RuII(bpy)$_3$]$^{2+}$ and 20 μL SPS stock solutions. The mixture was poured into different size Teflon molds according to the corresponding experimental requirements and was photosolidificated with 30 s irradiation of LED dental curing lights at room temperature. The different PH/GOG

Table 1
The concentration of gelatin and GOG in PH/GOG composites.

Sample name	Gelatin concentration mg/mL	GOG concentration mg/mL
PH	100	0
PH5	100	0.175
PH10	100	0.350
PH15	100	0.525
PH20	100	0.700
PH30	100	1.050
PH40	100	1.400
PH50	100	1.750

Table 2
Definitions of the relative parameters for tyrosine content analysis.

Parameter	Definition
$C_{TYR@GOG}$	The amount of tyrosine carried by GOG in per unit volume of PH/GOG composite.
ΔTYR^+	$C_{TYR@PH/GOG}^+ - C_{TYR@PH}^+$, represents actually detected changes in tyrosine content per unit volume of the composite due to the addition of GOG and the crosslinking after photopolymerization.
$\Delta\Delta TYR^+$	$\Delta TYR^+ - C_{TYR@GOG}$, represents the actual detected changes in tyrosine content per unit volume of the composite due to the covalent bond formation and the structural change caused by GOG without the amount of tyrosine carried by GOG.

samples with different concentrations of GOG were named as PH, PH5, PH10, PH15, PH20, PH30, PH40, and PH50, respectively. The compositions of each group of composites were detailed in Table 1.

The pre-crosslinked PH/GOG composites were first spread on a glass slide forming a thin layer with ~1 mm thickness, followed by photopolymerization and observation under an optical microscope (Eclipse Ti, Nikon, Japan). The morphology of the composites' internal structure was studied with SEM (S3400, Hitachi, Tokyo, Japan), and the samples were prepared by freeze-fractured in liquid nitrogen. The elastic moduli of the different composites were tested by the electronic universal testing machine (HY-0230, HENGYI, China) equipped with a 100 N load cell through conducting the constant strain-rate compression tests. The samples (10 mm diameter × 5 mm thickness) were performed in the air after removal from the Teflon molds. The composite's hydrophilicity was tested after lyophilization of the composites smeared on the subject slide, both the image and the value were recorded in all the groups. The cast disc samples (10 mm diameter × 5 mm thickness) of the composite hydrogel (PH/GOG) were also used to evaluate its characteristics in swelling and degradation, in which the samples were weighted in triplicate to reduce errors immediately after crosslinking (W0) and soaking in 10 mL PBS at 37 °C with various times (Wt). The weight change of the composites (Mass/%) was recorded according to the formula Mass/% = Wt/W0 and used to evaluate the degree of swelling and degradation. It is assumed to be the accomplishment of deterioration until the composites disappeared entirely with no remaining materials. XRD and FTIR spectrum of the composites were also conducted using the methods described above in the characterization of GO and GOG.

2.5. The tyrosine detection

To investigate and analyze the crosslinking interaction between gelatin and GOG, as well as inside structure of the PH/GOG composite, the tyrosine content of the composite after photopolymerization was detected. Briefly, 50 μL pre-crosslinked PH or PH/GOG composites (PH5, PH10, PH15, PH20, PH30, PH40, PH50) were respectively added in 96-well plate, the tyrosine content per unit volume of the composite after ($C_{TYR@PH}^+$ or $C_{TYR@PH/GOG}^+$) photopolymerization were both measured using a Tyrosine Colorimetric Assay Kit (MAK219, Sigma, USA) according to the manufacture's introduction. For a better calculation and analysis, we defined several parameters listed in Table 2. The

total amount of tyrosine carried by GOG, which is involved in per unit volume of PH/GOG composite ($C_{TYR@GOG}$), was calculated from the result of the mass ratio of tyrosine to GOG above mentioned. $C_{TYR@GOG}$ presented the theoretical increment of tyrosine due to the addition of GOG in the composites.

2.6. Cell viability and adhesion on the surface of the PH/GOG composites

The live/dead test was conducted to observe the viability of BMSCs after seeded on the hydrogel composites as previously described [36]. The BMSCs suspension with a density of 1×10^5 cells/mL was seeded on 150 μL composites that were photopolymerized in the cell culture dish with a glass bottom (Glass Diameter: 10 mm). The live/dead staining was carried as a manufacturer's protocol after seeding the BMSCs on composites 24 h culture. Besides, the cell adhesion on the composites was illustrated with two-time points (4 h and 6 h). The integrin immunofluorescent staining at 6 h were incubated with primary antibody (ab150361; Abcam, USA). After staining the cell with FITC-labeled phalloidin for cytoskeletal β-actin, the images were analyzed using CLSM (LEICA, Germany). CCK-8 assay was carried out for a quantitative analysis on the BMSCs viability after the cells were seeded with a density of 5000 cells/well and cultured on the composites at 1, 4, 7 and 14 d. The 50 μL of PH and PH/GOG composites (PH5, PH10, PH15, PH20, PH30, PH40, PH50) were added in 96-well plate with photo polymerization for the CCK-8 assay, and the procedure was carried according to the manufacturer's protocol to evaluate the cell viability.

2.7. Cell viability inside the PH/GOG composite

When BMSCs were mixed inside the composites with 5×10^5 cells mixed in 150 μL composites that were photopolymerized in a cell culture dish with 10 mm diameter glass bottom, the live/dead assay was also conducted using the methods described above. 3D Images of the composites mixed with BMSCs (about 120 μm in thickness) were recorded based on CLSM (LEICA, Germany). Lenti-luciferase transfected BMSCs were combined with different PH/GOG composites, and the mixtures were implanted in the back of nude mice subcutaneously for culture *in vivo*. After one week, the implants' luminescent images were acquired after injection of the luciferin substrates using the optical imaging system (Night-OWL LB 983, Berthold Technologies, Germany) to verify the *in vivo* viability of BMSCs mixed inside of the composites.

2.8. Intracellular nitric oxide detection

NO fluorescent probe (DAF-FM DA; Beyotime, China) was used to test the intracellular nitric oxide (NO) activity of BMSCs according to the protocol. NO fluorescence was recorded by microscope after the incubation of BMSCs that were adhered to or mixed in the composites with the DAF-FM DA (5 μM) for 20 min at 37 °C in darkness.

2.9. Fabrication of MV-loaded PH/GOG composite (PH/MV/GOG) and its osteogenic and angiogenic effects on BMSCs

According to our previous study [36], the composite of MV loaded GOG (MV/GOG) in saturated absorption state were prepared for the construction of PH/GOG composites. Various amounts of the prepared MV/GOG (0, 5, 10, 15, 20, 30, 40, or 50 μL of 35 mg/mL MV/GOG in PBS) were used instead of GOG to form the PH/MV/GOG composite which was named as PH, PH5M, PH10M, PH15M, PH20M, PH30M, PH40M, and PH50M, respectively. The BMSCs suspension with a density of 5×10^4 cells/mL was seeded onto 150 μL composite hydrogel photopolymerized in a cell culture dish with 10 mm diameter glass bottom to analyze the osteogenic effect of the composites. ALP staining, Runx2 immunofluorescence staining at 7 d, and Col1 immunofluorescence staining at 21 d were conducted according to the description in our previous research [36]. PCR assays were carried out to estimate the
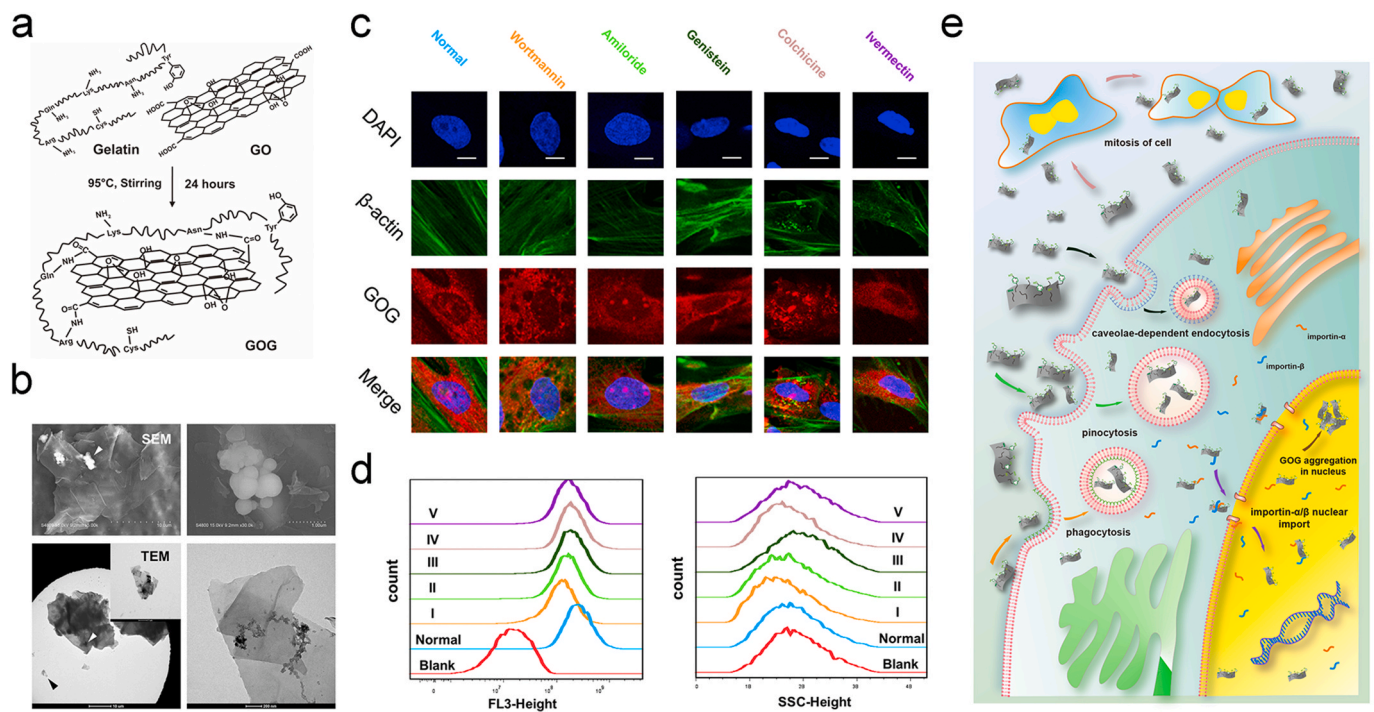
Fig. 2. Characterizations of GOG and the endocytosis of GOG in BMSCs. a) Schema of the preparation of GOG. b) SEM and TEM of GOG. c) The morphology evaluation by confocal laser scanning microscopy (CLSM) of cultured BMSCs after endocytosis inhibitors and the R6G labeled GOG treatment. Normal: BMSCs treated with DMEM containing R6G labeled GOG only. Bar: 10 μm. d) The quantity analysis of the endocytosis mechanisms. The five inhibitors were represented with I, II, III, IV, and V respectively, corresponding to the same color. Histograms of FL3-height (R6G intensity) in flow cytometry reflected the amount of R6G labeled GOG endocytosis in BMSCs under the action of inhibitors. Histograms of SSC-height revealed the cell complexity induced by R6G labeled GOG endocytosis in BMSCs under the effect of inhibitors. Blank: BMSCs treated with DMEM only. e) Schematic illustration of the endocytosis of GOG. (For interpretation of the references to color in this figure legend, the reader is referred to the Web version of this article.)

osteogenic markers' expressions of the BMSCs seeded on PH/MV/GOG composites at 7 d and 21 d. For analysis the angiogenic effect of the composites, a sprouting study was conducted by seeding BMSCs on the composites with a low cell density of 2.5×10^4 cells/mL, and the immunofluorescence staining of angiogenetic marker CD31 was carried out by incubation with primary antibody (ab24590; Abcam, USA) at 7 d. The total capillary branch lengths, the number of circles, and the number of nude points per field were identified and counted by NIH ImageJ 1.45 software. PCR was also performed for angiogenic markers Ang1, VEGF, vWF, and CD31 after culturing the 5×10^4 BMSCs on the composites for 7 d. The sequences of the used primers were described in the Supporting Information.

2.10. Mechanism of the PH/MV/GOG composite on the osteogenesis and angiogenesis

BMSCs were incubated on the different PH/MV/GOG composite (PH, PH5M, PH15M, and PH30M) to exam the change of the Erk1/2 and AKT signal pathway. After 12 h culture, the cell's total protein was collected with RIPA mixing with phosphatase inhibitor cocktail and analyzed the expressions of p-Erk1/2, Erk1/2, p-AKT, AKT, and Mcl1 by Western blot. The protein expressions of Runx2 and VEGF were tested after 7 d culture. The expressions of OCN and OPN were measured after 21 d culture. Primary antibodies against p-Erk1/2 (#4370, CST, USA), Erk1/2 (#4695, CST, USA), p-AKT (#4060, CST, USA), AKT (#4691, CST, USA), Mcl1 (ab32087; Abcam, USA), Runx2 (ab23981; Abcam, USA), VEGF (ab1316; Abcam, USA), OCN (sc-390877; Santa, USA), OPN (ab8448; Abcam, USA) and β-actin (ab8227; Abcam, USA) were used in our study. Rat BMSCs were incubated in a culture medium containing 10×10^{-6} M PD98059 (#9900, CST, USA), the Erk1/2 signal pathway inhibitor, to confirm that the up-regulated Runx2 and VEGF expressions resulted from the activation of the Erk1/2 signal pathway.

2.11. Preparation of implants for the repair of rat critical-sized calvarial bone defect

The composites of PH/MV, PH15, PH15M, PH + BMSCs and PH15M + BMSCs were poured into a Teflon mold and photopolymerized to form the implants (5 mm diameter × 2 mm thickness) under sterile conditions. Rat critical-sized calvarial bone defect [43] was conducted to test the repair effects of different PH/MV/GOG composites after implantation, in which 24 rats with an average weight of 300 g and an age of 12 weeks were used for tests in vivo. Two full-thickness round defects with 5 mm diameter were created on both sides of the rat skull; null, PH/MV, PH15, PH15M, PH mixed BMSCs (PH + BMSCs) and PH15M mixed BMSCs (PH15M + BMSCs) were implanted in both defects and divided into null-PH/MV, PH15-PH15M, and PH mixed BMSCs-PH15M mixed BMSCs three groups. Eight rats were set as a group that was embedded with a group of implants described above, so all the rats would be randomly divided into three groups with different implant groups. We would sacrifice half of the animals at 4 weeks and 8 weeks respectively, after implant surgery. The microangiography was carried out to evaluate the vascularization at 4 weeks as previously described [44]. The sequential fluorescent labeling was carried out for the 8 weeks collected animal groups with intraperitoneal injection 35 mg/kg Alizarin Red S (AL), 30 mg/kg Calcein (CA), and 30 mg/kg Tetracycline Hydrochloride (TE) at 2, 4 and 6 weeks respectively.

2.12. Micro-computed tomography (μCT) and histology analysis of the bone repair

The harvested bone samples were scanned with μCT (GE Explore Locus SP microCT, USA) to evaluate the formations of new bone and new blood vessels. The 3D reconstructions of the bone and blood vessels were made to illustrate the bone repair effect. Besides, a cylinder area

involving the defect site with a height of 5 mm and a diameter of 5 mm was selected as the VOI in which the total vessel volume and the newly formed bone were quantified as several parameters to reflect the properties of the new bone. After μCT analysis, the fixed bone samples without vascular perfusion at 8 weeks were assigned to histological analysis. The tissue sections were prepared into 5 μm thickness parallel to the long axis of the skull; meanwhile, hematoxylin/eosin (HE) and Masson trichrome staining were performed to show the different repair results of the implants. The quantified analysis of the bone formation in Masson stain was illustrated by the ratio of mature bone to the osteoid matrix by the NIH ImageJ 1.45 software. The non-decalcified skull specimens were used to observe the sequential fluorescent labeling, as previously described [45]. Additionally, immunofluorescence staining of CD31 in the sections was performed as a similar procedure described above and was subjected to a fluorescence microscope for recording the images followed by treatment with HE and mounted finally. The fluorescence intensity of CD31 was analyzed by the NIH ImageJ 1.45 software.

2.13. Statistical analysis

Statistical comparisons were conducted by one-way ANOVA and SNK post hoc analysis after the normal distribution and equal variance assumption test. The results were expressed as means $\pm$ SD, and the statistical analysis was performed by SAS 8.2 statistical software package (Cary, USA). The differences were considered statistically significant at the confidence levels above 95% ($p < 0.05$).

3. Results and discussion

3.1. The endocytosis and distribution of GOG in BMSCs

As we reported previously [36], the GOG that we prepared from the GO and gelatin, showed better stability (Figure S2a, Supporting information). The changes in the particle size and zeta-potential suggested that the gelatin immobilization on the graphene oxide made its particle size larger and negative charge lesser after reduction by gelatin (Figure S2b, c, Supporting information). The XRD and FTIR analysis (Figure S2d, e, supporting information) showed the difference between the GO and GOG. The GOG got from the reduction of GO no longer showed the characteristic peak of the oxidation state at 10 ° in the XRD spectrum. During the preparation of GOG, Asparagine (Asn), Glutamine (Gln), Arginine (Arg), and Lysine (Lys) with –NH$_2$ groups in the gelatin maybe interact with the –COOH in the surface of GO to constitute GOG (Fig. 2a). Furthermore, the SEM and TEM presented the flake-like structure of GOG nanosheets; meanwhile, the winkled and curled fabric also could be observed (Fig. 2b). The sphere aggregations on the surface might derive from gelatin, and the high-resolution TEM proved that the gelatin immobilized on GOG appearing as black dots and the long chain of gelatin on the surface of GOG. Combining with the results about the tyrosine content of the GOG and GO tested by the Tyrosine Colorimetric Assay kit (Figure S2f, Supporting information), which demonstrated that 1 μg GOG loaded 4.882×10^{-3} nM Tyrosine and the content of tyrosine in GO was approximate to zero, we could confirm that the GOG had the gelatin in its surface and could participate in the tyrosine covalent bond formation.

We have reported that the GOG could enter BMSCs and distribute extensively, both in the nucleus and cytoplasm [36]. For further analysis of the endocytosis mechanism in BMSCs, the R6G-labeled GOG was prepared and clarified to be labeled successfully. Meanwhile, the light view of the endocytosis GOG in BMSCs was also captured (Figure S2g, Supporting information). Endocytosis, a cellular process in which substances are brought into the cell, usually includes phagocytosis (cell eating), pinocytosis (cell drinking), and caveolae-dependent endocytosis. As a bioactive nanomaterial, the GOG could enter the cell and elicit some impacts to regulate the specific biological activities. The detailed

mechanisms of the endocytosis and the nanomaterial distributions in the cell were correlated with the exertion of its bio-functions.

In our study, the BMSCs treated with several inhibitors showed the different distributions of GOG, which illustrated the different roles of these endocytosis mechanisms in the uptake of GOG (Fig. 2c). The block of phagocytosis using wortmannin in BMSCs showed the absence of GOG in the small vacuoles, also known as wortmannin compartments, which resulted from the inhibited further transport of vesicles [46] due to inhibition of the phosphatidylinositol (PI) 3-kinases by wortmannin [47]. The amiloride treated BMSCs also showed the small vacuoles that did not contain GOG due to the block of pinocytosis by inhibiting Na$^+$/H$^+$ exchanger [40]. Due to the G1 arrest of the cell cycle by amiloride, the Cajal body showed heterogenic distributions in the nucleus [48]. Meanwhile, the GOG distribution in the core also showed the same pattern of heterogenic distribution as the Cajal body, implying that GOG may be localized in the Cajal body to regulate its functions. Recent research showed that the Cajal body could process siRNA, miRNA, and pre-mRNA to regulate the RNA function [49,50]. Meanwhile, the osteogenesis and angiogenesis were also influenced by the RNA function [51,52], from which it could be deduced that GOG may exert its bio-functions by altering the RNA function. The inhibited caveolae-dependent endocytosis by genistein also affected the endocytosis of GOG. The small vacuoles without GOG could be identified in the BMSCs due to the inhibition of Src tyrosine kinases and caveolae dynamics [41]. The cell treated with colchicine for 2 h showed an uneven distribution of GOG, implying that the disturbed cell cycle influenced the endocytosis and delivery of GOG in BMSCs. The influx of GOG into the nucleus was decreased by the treatment of ivermectin, which inhibits the importin α/β-mediated nuclear import [42]. This phenomenon showed that the nuclear import of GOG was related to the importin α/β, which translocated the substances with atomic localization signals into the nucleus through nuclear pore complexes (NPC). We further quantitatively measured the cellular uptake of GOG at 2 h using flow cytometry. The flow cytometry dot-plot image indicating the distribution of SSC-Height and FL3-Height (R6G) intensities presented the difference between the standard and treated groups with different inhibitors (Figure S2h, Supporting information). The quantity analysis of the endocytosis mechanisms (Fig. 2d) showed that the BMSCs operated by wortmannin and amiloride presented a significantly decreased uptake of GOG (decreased FL3-Height). Additionally, the genistein, colchicine, and ivermectin also slightly inhibited GOG endocytosis by affecting the caveolae dynamics, microtubules, and importin-α/β, respectively. The SSC parameter, which reflected cell complexity, was related to many factors, such as size and number of the particles in the cell, organelle distribution in the cell, and the other factors. The SSC-Height (Fig. 2d) indicated the same trend effect of the inhibitors on endocytosis of GOG as FL3-Height, except genistein and ivermectin. The break of caveolae dynamics and the abnormal function of importin due to genistein and ivermectin may result in the cell's unusual physiological activity, which induced an increased granular complexity of BMSCs with the decreased endocytosis of GOG (decreased FL3-Height). The SSC-Height of the cell treated by wortmannin, amiloride, and colchicine were reduced due to the inhibited endocytosis of GOG. The schematic illustration (Fig. 2e) showed the track of GOG corresponding to the same color inhibitors. The analysis of the endocytosis and distribution of GOG in BMSCs showed its excellent biocompatibility, which promised essential biological functions.

GOG as a good nanocarrier for bioactive factors, and the endocytic process of GOG in BMSCs was mainly through the phagocytosis and pinocytosis pathways for the uptake of GOG. Furthermore, we have known that graphene and graphene-based materials could promote osteogenic [15–17] and angiogenic [18] differentiation of the mesenchymal stem cells *in vitro*. Combining with the results of tyrosine content that showed the presence of gelatin on the GOG, we hypothesized that GOG could not only function as the nanocarrier for bioactive factors but also act as a filler to react with gelatin through the tyrosine involved
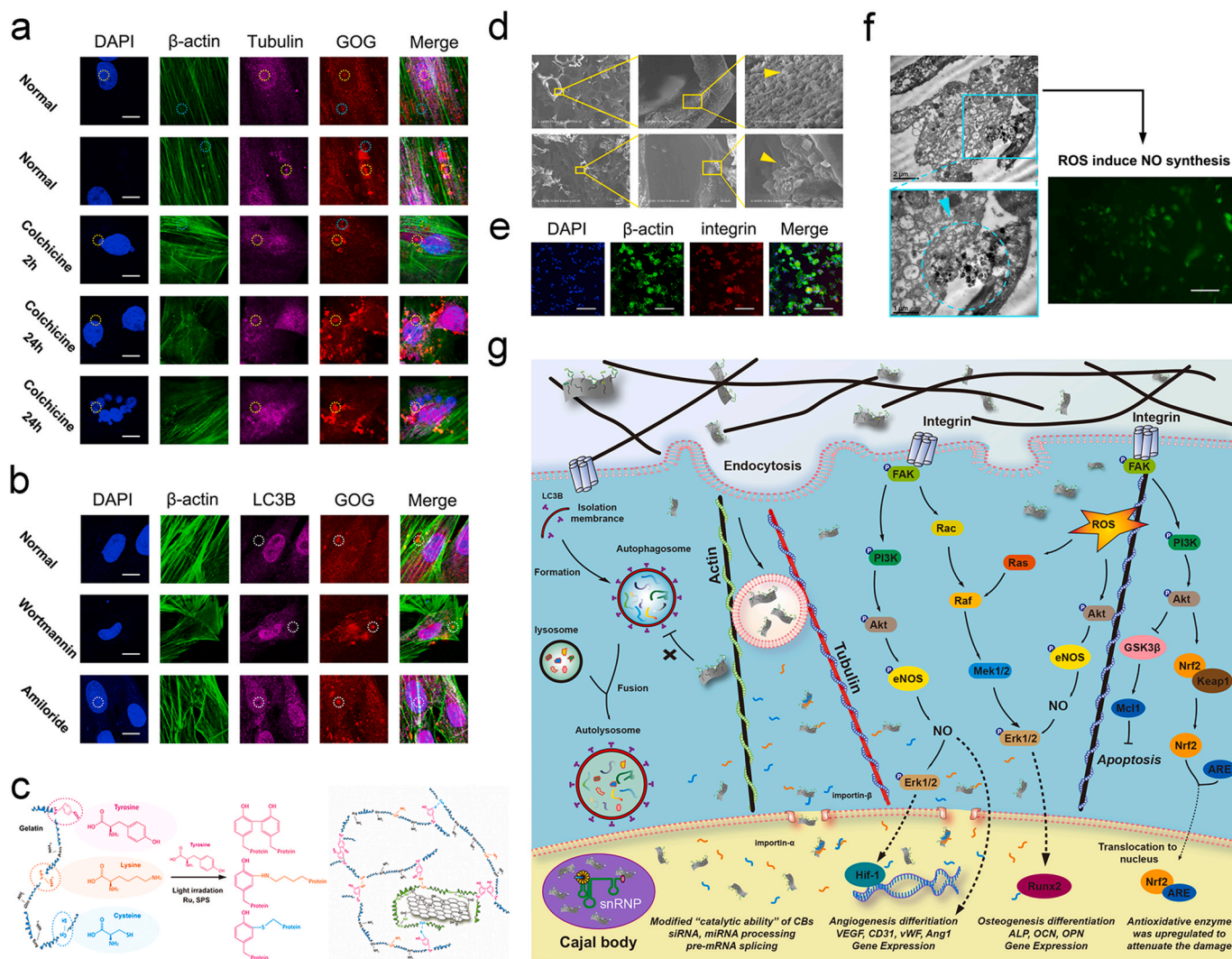
Fig. 3. Biocompatibility of GOG and the biological functions of biomimetic procallus. a) Effect of colchicine treatment for different time on the endocytosis and distribution of R6G labeled GOG in BMSCs. Yellow and blue dot circles indicate the same site in each channel. Bar: 10 μm. b) Effect of wortmannin or amiloride treatment on the autophagocytosis and distribution of R6G labeled GOG in BMSCs. White dot circles indicate the same site in each channel. Bar: 10 μm. c) Schematic illustration of the mechanism of the photo-initiated crosslinking reaction. d) The SEM of the section view of the composite with GOG. e) Integrin immunofluorescence staining of the BMSCs seeded on the composite at 6 h. Bar: 50 μm. f) TEM images showed the endocytosis of GOG in BMSCs and the NO synthesis caused by GOG. Bar: 250 μm. g) Schematic illustration showed the mechanism of biomimetic composites. (For interpretation of the references to color in this figure legend, the reader is referred to the Web version of this article.)

covalent bond for further improving the mechanical properties of the composites and eliciting its osteoinductive and angio-inductive bio-functions. The GOG reinforced composite maybe also mimics the pro-callus for the rapid and excellent repair of the bone defect.

3.2. The biological functions of GOG and biomimetic procallus

To further analyze the influences of GOG on the vital cellular activities, we examined the mitosis and autophagy of BMSCs with GOG incubation. Analysis of the endocytosis of GOG in BMSCs treated by colchicine for 2 h had shown that the disturbed cell cycle influenced the distribution of GOG in the cell. For further study on the interrelationship between the cell cycle and uptake of GOG, we pre-treated BMSCs with colchicine for 24 h to analyze the endocytosis of GOG. The tubulin immunofluorescent staining of normal BMSCs without treatment with colchicine showed that GOG had the partial co-localization with the tubulin in both nucleus and cytoplasm (Fig. 3a, Yellow dot circle). It means that the GOG has the interlace with the tubulin, which implies that the transport of GOG maybe relates to the tubulin. It's worth

mentioning that the β-actin also showed co-localization with GOG (Fig. 3a, Blue dot circle) besides the co-localization of GOG with tubulin, which indicated that the interaction between the actin and GOG mediated the transportation of GOG. The BMSCs treated with colchicine for 2 h showed little difference in the position relationship between the tubulin and GOG from the normal BMSCs, except for the uneven distribution of GOG. Furthermore, the uneven distribution of GOG in BMSCs treated with 24 h was obvious, and the partial co-localization of the tubulin and β-actin with GOG also could be identified in the BMSCs with the disturbed cell cycle. A previous study demonstrated that graphene-based materials could directly influence the cytoskeletal organization by affecting cytoskeletal tension, resulting in cell differentiation [53]. Our results showing the co-localization of GOG with cytoskeletal implied that GOG could regulate the differentiation of BMSCs. Although the cell cycle was disturbed by colchicine, the distribution of GOG in BMSCs was also extensive, and the abnormal shape and number of nucleus didn't affect the distribution of GOG in the nucleus (Fig. 3a, Yellow dot circle), which indicated the biocompatibility of GOG. Meanwhile, the LC3B immunofluorescent staining of BMSCs
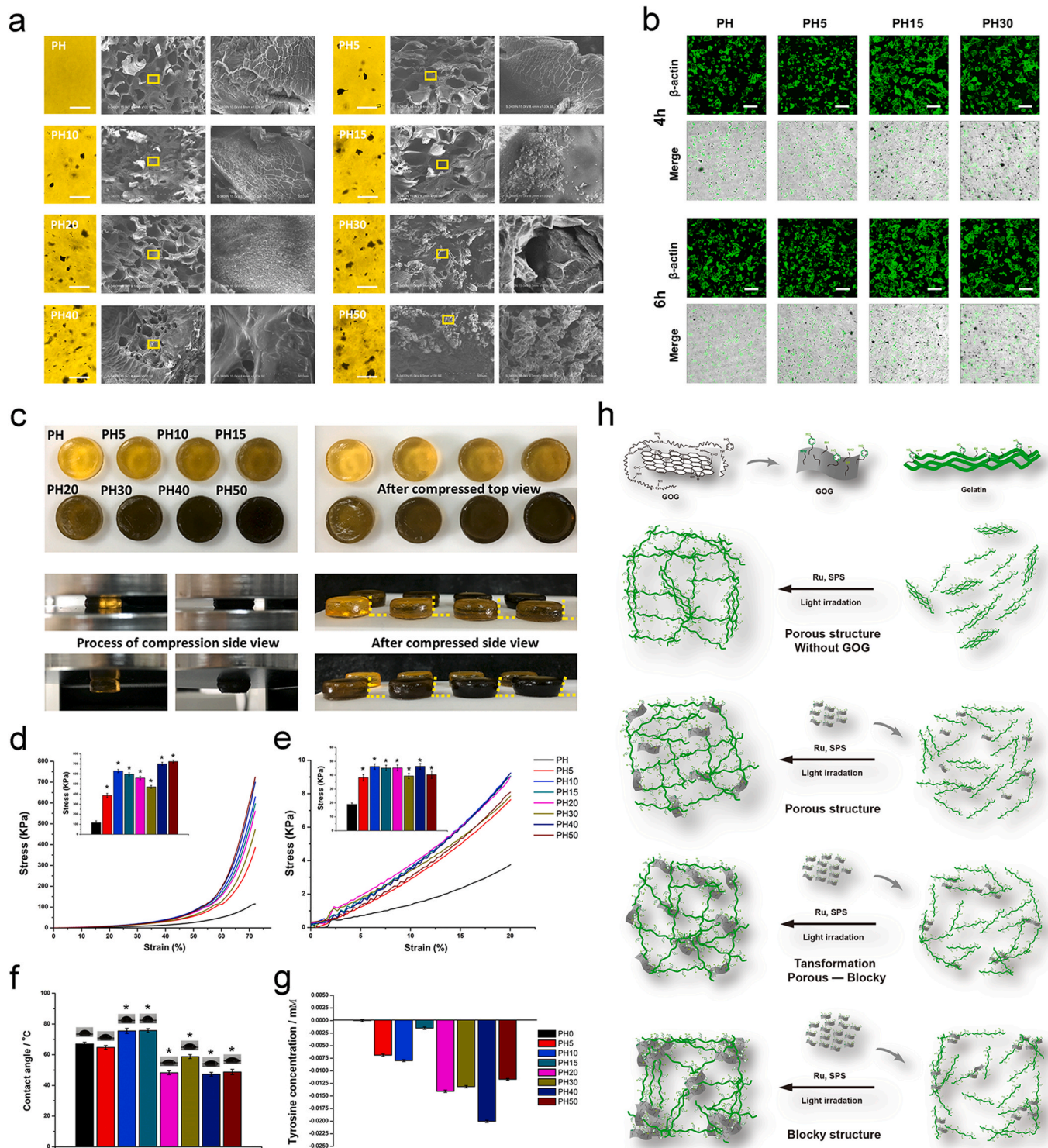
Fig. 4. The biomimetic microstructure of the composites modulated by GOG. a) The SEM of the section view of the composite with the light view of the hydrogel. Bar: 100 μm. b) The adhesion of BMSCs on the composite after seeding for 4 h and 6 h. Bar: 100 μm. c) The digital photos showed the mechanical property of the composites. The yellow dot lines show the deformation of the gel after the compression. d) The stress-strain curve and the compression strength at the strain of 72%. *: $p < 0.05$ versus PH. e) The linear region of the stress-strain curve and the compression modulus at the strain of 20%. *: $p < 0.05$ versus PH. f) The contact angle of the composite. *: $p < 0.05$ versus PH. g) The changes of the differential values with irradiation ($\Delta\Delta TYR^+$). h) Schematic illustration of the structural transformation of the composites with the increased GOG. (For interpretation of the references to color in this figure legend, the reader is referred to the Web version of this article.)

showed that GOG would not give rise to the aggregation of LC3B, and it also did not show co-localization with LC3B (Fig. 3b, White dot circle), which implied that the GOG endocytosed by BMSCs did not induce the formation of autophagosome and had the opportunity to exert its

functions with good biocompatibility.

On the whole, the immunofluorescent staining of LC3B and tubulin showed that the GOG did not intrigue the damage from autophagocytosis, and the mitosis of the cell did not influence the distribution of GOG

in cells. The excellent performance of GOG in the cell further promised the potential for delivering growth factors. Graphene alone can cause oxidative stress and cytotoxicity in tissue engineering regeneration [54, 55], so we use graphene in combination with other materials to reduce its side effects and guarantee its potential in promoting stem cell proliferation and differentiation [12,15]. Additionally, the pure photo-crosslinked hydrogel, due to the limitation of mechanical strength, is restricted as an ideal material with the lack of osteogenesis [56]. To overcome the mechanical limitation, we constructed the biomimetic composites by mixing the inorganic GOG with photo-crosslinked gelatin hydrogel. The GOG could help protect the composites from damage by stress distribution, thus relatively increasing the mechanical strength of the composite [57].

The GOG reinforced photo-crosslinked composites could mimic the reparative phase of bone healing with the delivered growth factor. The construction was composed of the interaction between the ingredients resulting in the achievement of biomimetic procallus for promoting bone healing. Compared with the gold standard of bone repairments, autologous bone graft (ABG), the biomimetic procallus resembles the early reparative stage of bone healing and could elicit the subsequent repairing and remodeling processes with the active and fast biological responses other than the inactive bone remodeling in ABG (Fig. 1a). So, the biomimetic composites derived from the realm of developmental engineering would potentially result in extensive bone regeneration (Fig. 1b). The gelatin immobilized on GOG offered a bionics nucleation site where the inorganic mineral substance interlaced with the organic matrix substance, like the crosslink between collagen and the mineralized hydroxyapatite. So, the GOG could be mixed with photo-crosslinked gelatin hydrogel to construct the biomimetic materials. The schematic illustration showed the mechanism of the photo-initiated crosslinking reaction between tyrosine, lysine, and cysteine on the GOG and gelatin (Fig. 3c). The photo-crosslink principle made the composites form more covalent bond crosslinks to reinforce the mechanical properties and regulate the hydrogel structure. The internal structure of the composites incorporating GOG was observed by SEM (Fig. 3d). The images exhibited that the GOG reinforced composites with a porous microstructure appeared as the distribution of nanoparticles on the wall of holes. The GOG mixed with the gelatin also could distribute in the interior portion of the hole walls, as presented in the lower row of SEM. Due to the high ultimate strength of the graphene-based material, GOG also could reinforce the mechanical properties to the appropriate range for better biological functions. The immunofluorescence staining of integrin, cell adhesion receptor, in the BMSCs (Fig. 3e) after seeded on the composite for 6 h, showed the suitable attachment of BMSCs on the surface of the composite with healthy cell spreading, which resulted from the proper microstructure of the composite. The adequate adhesion for BMSCs on the composites could guarantee a good proliferation on the composite without apoptosis. In the high-resolution TEM (Fig. 3f), the process of the endocytosis of GOG in the BMSCs was presented. The small vacuoles in the TEM were observed, showing the endocytic process of GOG by BMSCs, which was consistent with the results of confocal images. The ROS caused by GOG could induce NO synthesis, which promoted the angiogenic differentiation of the stem cells. The ROS caused by GOG was just like a double-edged sword, the low level of ROS had a mimetic effect of the hypoxic microenvironment in the inflammatory stage to exert the bioactive signals for repair, but the high-dose of ROS would have the damage to the cells [18]. Overall, the photo-crosslinked gelatin hydrogel with GOG could construct a biomimetic extracellular matrix microenvironment for the effective utilization of the ROS. The appropriate hypoxic microenvironment caused by GOG reinforced composite could also exert its biological effect through ROS induced NO synthesis (Fig. 3f).

With the developmental engineering design, the hypoxia microenvironment induces the angiogenesis in the biomimetic composites to establish a nutrient-rich intermediated condition. Meanwhile, the bioactive factors that come from the GOG delivery and the secretion of

the primed progenitor cells integrate with the GOG-modulated composite structure and the angiogenesis of the biomimetic composites to construct a dynamic process for the subsequent reparative and remodeling stage of the bone healing. The biomimetic composites with the porous structure, suitable mechanical property, and bioactive signals system could mimic the fibrocartilaginous ECM (procallus) for bone repair. As showed in the Schematic illustration (Fig. 3g), the biocompatibility of GOG and the composite induced bioactive signals in the BMSCs promised a prospect of the biomimetic procallus for bone repair. The co-locations of GOG with tubulin, actin, and Cajal body, as described above, implied its biocompatibility. The escape of GOG from the autophagosome also made it an ideal nanocarrier for bioactive factors. The adhesion of BMSCs on the composite would initiate the sequent signal transduction to activate the Erk1/2 pathway and the PI3K/AKT pathway for regulating the osteogenesis and angiogenesis [58,59]. Meanwhile, the proper ROS level in the cell could also induce the activation of the Erk1/2 and PI3K/AKT pathway to exert its biological functions [60], which mimics the initial inflammatory phase with hypoxia condition to induce the angiogenesis. During the signals transduction, the activation of the Erk1/2 pathway could induce the angiogenic and osteogenic differentiation of the BMSCs by Hif-1 [61] and Runx2 [59], respectively. The activation of the AKT pathway could mediate the eNOS phosphorylation to initiate the NO synthesis for angiogenesis [62]. At the same time, the phosphorylation of GSK3β by PI3K/AKT could inhibit apoptosis by increasing Mcl's expression [63]. Besides, the PI3K/AKT pathway could promote the expression level and amount of antioxidative enzymes by increasing Nrf2 protein levels in the nucleus, exerting the antioxidant role [64]. Overall, the proper extracellular matrix microenvironment and the ROS level in the biomimetic procallus could promote the adhesion, proliferation, and differentiation of the progenitor cells, which all the advantages for the regeneration come from the pivotal role of GOG. The excellent biocompatibility and bionic regulation effects of GOG give the BMSCs a favorable environment to repair the defect.

3.3. The biomimetic structure of the GOG reinforced procallus

The biomimetic microstructure of the composite was the primary condition for the subsequent repair and regeneration. The specific geometric configuration of the substrates could regulate the differentiation of stem cells for tissue engineering [65–67]. For analyzing the effect of GOG on the structure and biological functions of the biomimetic procallus, we constructed a series of composites with different ratios of GOG. The composites with a proper amount of GOG integrated the advantages of gelatin and GOG, which provided a better structural morphology of the biomimetic procallus and exhibited osteogenic and angiogenic effects on the BMSCs. The SEM showed the structural change of the composites, which transformed from the porous to blocky structure (Fig. 4a). Meanwhile, the adhesion of BMSCs on the surface of the different composites showed the difference, which indicated that the ratio of GOG in the composite played a critical factor in regulating the structure and biological functions (Fig. 4b). The PH15 composite showed the proper porous structure and promoted the adhesion of BMSCs on it. Further analysis of the effects of GOG ratio on the regulation of the mechanical properties showed that the PH15 had the best mechanical properties. The upper row of the digital photos (Fig. 4c) showed the composites' view before and after the compression test. Besides, the yellow dot lines in the low row showed the deformation of the composites after the compression test. The compression strength of composite hydrogels at 72% strain increased significantly, with the concentrations of GOG increasing to PH10 and then decreased gradually from PH15 to PH30. Lastly, the PH/GOG composites exhibited an extraordinary increase of the strength with the addition of GOG once more (Fig. 4d). The compressive modulus of the composites at 20% strain also showed the regular trend of results, which was similar to the compression strength except for the decrease in PH50 (Fig. 4e). The best

resistant ability of the PH50 and the decreased compressive modulus compared to PH40 were consistent with the structural transformation from the porous microstructure to the blocky structure. The proper construction of PH15 showed suitable mechanical properties within the kPa range that was reported to be ideal for the cell adhesion and differentiation [68,69]. The hydrophily of the hydrogel composites (Fig. 4f) illustrated that the hydrophily of the composites became weaker with the increasing GOG before PH15. The hydrophilicity became better with a further increase of GOG, which may be due to the microstructure change of the composites from porous to the blocky organization, in which the best stretch of the porous microstructure in PH10 and PH15 after lyophilization contributes to the poorest hydrophilicity.

The gelatin immobilized on GOG guarantees it to participate in the formation of the tyrosine involved covalent bonds. Furthermore, the covalent bond formation between the tyrosine and tyrosine, lysine, and cysteine would block the tyrosine to reacted with the Tyrosine Colorimetric Assay kit, which resulted in the decrease of the detected tyrosine. So, the tyrosine content detected by Tyrosine Colorimetric Assay kit would show a different pattern with the increased amount of GOG mixed in the composites, which regulates the structural transformation of the composites from the porous structure to the blocky structure. After the irradiation, the change of tyrosine concentration in PH/GOG composites reflected the influences of the crosslinked covalent bond formation and the structure transformation (Fig. 4g). The formation of tyrosine involved covalent bonds after photo-crosslinking caused the decrease of the detected tyrosine, while the structural transformation of the composites would induce different changes of the detected tyrosine. When the porous structure was reinforced with the increased GOG, the detected tyrosine was increased due to the stretch of the porous structure with more exposure of tyrosine to react with the kit. With the further increase of GOG, the structural transformation from porous to blocky resulted in a decrease in the detected tyrosine because of the structure's contraction. Compared with PH composite, the GOG caused more tyrosine covalent formation in the PH/GOG composite resulting in the negative value of $\Delta\Delta TYR^+$ (Table 2 shows the definitions of the relative parameters for tyrosine content analysis). The tyrosine pattern showed a regular variation trend, which was similar to the modulus' changing pattern. The schematic illustration (Fig. 4h) showed the hypothesis of the structural transformation. Through combining the results of SEM and mechanical properties with the detected tyrosine concentration change, it could be speculated that the PH10 and PH15 composites were the best setups of gelatin hydrogel and GOG. With the further increased GOG, the structure of the composites began to transform to the blocky organization, and the GOG became the principal part instead of the gelatin hydrogel with a decreased modulus. The composites' swelling properties also showed the PH15 had better swell-degradation performance (Figure S3a, Supporting information). The XRD and FTIR results of the composite showed no difference in the pattern between the curve of PH, PH5, PH15, and PH30, except for a little difference in the intensity of several specific positions (Figure S3b, c, Supporting information). All of the results are consistent with the previous research, concluding that the original properties of the matrix, the size, form, and content of the filler, and the interactions between the filler and matrix, can affect the features of the composites [57]. In conclusion, the biomimetic procallus with proper ratio of GOG showed the porous structure and promoted the adhesion of BMSCs on the composites. The PH15 composite maybe has the appropriate ratio of GOG for the better structure. Meanwhile, it could also elicit a sequence of bioactive signals for its biological functions to mimic the procallus.

For mimicking the progenitor in the procallus, the stem cell-based therapeutic (SCBT) strategies should be applied to provide an additional osteogenic potential of the implants compared to the acellular materials, which resembles the bioactive procallus that construct a semi-autonomous stem cell differentiation microenvironment for supplementary progenitor's recruitment from surrounding host tissue.

Emerging evidence suggests that quick stimulation of progenitor cells may improve the differentiation and gene expression of the stem cells compared to the untreated cells [70]. So, we need to select a bioactive factor to prime the osteogenesis of progenitors. In current studies, the researchers usually used the purified growth factors (e.g., BMP2, PDGF) [71] or the extraction of the endogenous tissue (e.g., PRP) for stimulating the osteogenesis of progenitors. These factors would facilitate bone regeneration through IM ossification other than EC ossification due to its osteoinductive and osteoconductive effects. Due to the hypoxic condition caused by GOG in the biomimetic procallus has mimicked the inflammatory stage favoring the EC ossification, we need to select the osteoinductive bioactive factor to facilitate the direct osteogenesis for IM ossification. By combining the EC ossification with IM ossification, we could regenerate the defects based entirely on the construction of biomimetic procallus. For improving the osteogenesis of biomimetic procallus, we selected MV as the bioactive drug loaded in GOG to prime the osteogenesis of the progenitors. In the further investigation on the bio-functions of the biomimetic procallus, we constructed a series of photo-crosslinked composites with different ratios of MV/GOG, which had the different mechanical properties, osteogenesis, and angiogenesis capacities. We would clarify the specific ratio of MV/GOG in the biomimetic procallus for eliciting its best biological functions and analyze its specific mechanism for promoting the bone repair.

3.4. The biological functions of MV/GOG reinforced procallus on osteogenesis and angiogenesis

In the native bone healing of the critical-sized bone defects, the inherent large bone defect is suitable for the chondrogenesis of bone repair due to the lack of blood supply. So, the EC ossification plays a primary role in the reparative phase of bone healing other than the IM ossification that needs an adequate blood supply. The study showed that the amount of new bone formation was related to the pattern of osteogenesis, and the implants facilitating IM ossification presented a more massive formation of new bone than EC ossification [72]. So, a majority of strategies have devoted to stimulating progenitor cells directly osteogenic differentiation rather than endochondral calcification, the implant conditions primed the direct osteogenesis guaranteeing an efficient bone repair. Meanwhile, the angiogenesis in the EC ossification could provide a better situation for the further IM ossification, which shows that both ossifications play an essential role in bone healing. For further constructing a better bioactive signals system combining the EC ossification with the IM ossification, we utilized the GOG as a nano-carrier to further expand its application in priming osteogenesis in addition to its effect of mimicking the hypoxia condition. The drug loading capacity of GOG is tested by Methyl vanillate, which is a new small molecule drug extracted from Hovenia Dulcis Thunb (HDT), which could induce activation of the Wnt/β-catenin pathway and promote the osteogenic differentiation [73]. HDT is a traditional Chinese plant medicine and used to treat fever, liver diseases, and hangover treatment [74]. It was reported that the proper concentration of MV could repair the femoral bone defect of ovariectomized mice through oral administration, in which the therapeutic effects were equivalent to that treated with an intraperitoneal injection of PTH(1–34) [73]. In the meanwhile, MV could promote osteogenesis without the risk of osteosarcoma accompanying with BMP and TGF signal pathway [75–77]. So, the growth factor MV loaded by GOG could accompany with the effect of the composites to promote the osteogenesis through activation of the Wnt/β-catenin pathway. The loading of MV on GOG (MV/GOG) had been reported as 1.5 μg of MV corresponding to 1 mg of GOG in saturated absorption condition in our previous research [36], and the MV release profiles from GOG exhibited that GOG showed a rapid release in the first 5 h with a subsequent sustained release of MV (Figure S3d, Supporting Information). Furthermore, the release of MV was nearly 65% at pH 2, which was more than that of approximately 50% at pH 7 after 30 h. The more hydrogen bond dissociation in the acidic
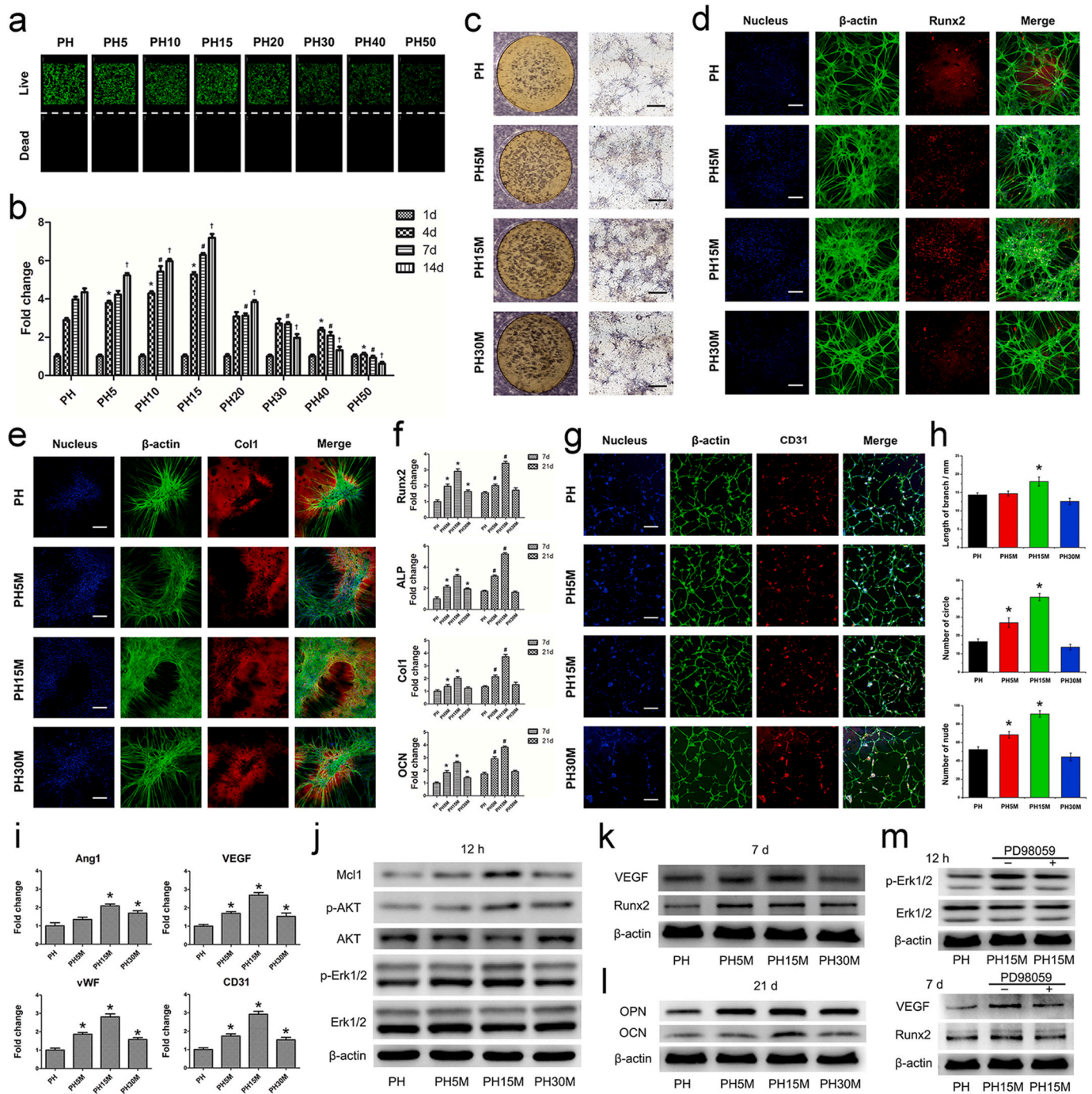
Fig. 5. Bi-differentiation of BMSCs on the MV/GOG reinforced procallus. a) The live/dead of the BMSCs seeded on the PH/GOG composites. b) The proliferation of the BMSCs seeded on the PH/GOG composite tested by CCK-8 kit. *: $p < 0.05$ versus PH at 4 d; #: $p < 0.05$ versus PH at 7 d; †: $p < 0.05$ versus PH at 14 d. c) The ALP staining of the BMSCs seeded on the PH/MV/GOG composites at 7 d. Black bar: 500 μm. d) Runx2 and e) Col1 immunofluorescence staining of the BMSCs seeded on the PH/MV/GOG composites at 7 d and 21 d respectively. White bar: 200 μm. f) Osteogenic differentiation related genes expression, such as the expression of Runx2, ALP, Col1 and OCN in BMSCs seeded on the PH/MV/GOG composites at 7 d and 21 d. *: $p < 0.05$ versus PH at 7 d; #: $p < 0.05$ versus PH at 21 d. g) The immunofluorescence staining of CD31 of BMSCs seeded on the PH/MV/GOG composites at 7 d. Bar: 200 μm. h) The quantitative analysis of the total capillary tube lengths, the number of circles and nude points per field. *: $p < 0.05$ versus PH. i) Relative gene expression of angiogenic marker Ang1, VEGF, vWF and CD31 in BMSCs seeded on the PH/MV/GOG composites at 7 d. *: $p < 0.05$ versus PH. j) The Western blot assays of the related pathway proteins and Mcl1 in BMSCs were analyzed after seeding on the PH/MV/GOG composites for 12 h. k) The expression of VEGF, Runx2 at 7 d and l) OPN, OCN at 21 d were also analyzed to test the osteogenic and angiogenic effects of the PH/MV/GOG composites. m) Inhibition of Erk1/2 signal pathway blocked the osteogenic and angiogenic properties of the PH/MV/GOG composites.

environment could explain why more MV release from GOG in pH = 2 [78]. Since the microenvironments of trauma and repair sites were more acidic than the typical humoral environment, which implied that more drug would be released from GOG for the therapeutic regimen [79]. This

acidic microenvironment caused by hypoxia conditions could induce the rapid drug release from GOG for priming the osteogenesis of the progenitors.

Before the evaluation of the biomimetic procallus for bone repair *in*

vivo, we firstly survey its biocompatibility on BMSCs *in vitro*. The biomimetic procallus, composed of GOG and photo-crosslinked gelatin, showed proper mechanical properties as described above, which may promote the adhesion and proliferation of progenitor without the cytotoxicity. The cell viability of BMSCs seeded on the PH/GOG composites were investigated by live/dead staining and CCK-8 assay. The results of live/dead staining (Fig. 5a) presented that the composites with different ratios of GOG showed no cytotoxicity at 1 d. The amounts of the cell adhering on the surface of the different composites were variant in the live/dead. Consistent with the results of the cell adhesion (Fig. 4b), the composite of PH15 showed the most amount of BMSCs in live/dead staining, which indicated that the better microstructure of the composites was suitable for the adhesion of the BMSCs on the surface of the hydrogel. The CCK-8 result (Fig. 5b), which measured the mitochondrial metabolic activity of BMSCs cultured on the composites, showed the change of the cell number to reflect the proliferation of BMSCs, with time from 1, 4, 7, and 14 d. The results indicated that the PH15 composite with a proper ratio of GOG had the best effect on promoting cell proliferation than other composites. Noteworthy, the PH15 composite maybe has the optimal concentration of GOG for cell adhesion and growth, which promises the potential sequent differentiation of the BMSCs.

Along with the excellent biocompatibility of the procallus, the proper hypoxic microenvironment caused by GOG resembled the initial inflammatory hematoma stage for eliciting bioactive signals in cellular development and tissue regeneration. The hypoxic microenvironment in the biomimetic procallus may favor the EC ossification for the bone fracture healing. Meanwhile, the MV delivered by GOG could induce direct osteogenesis to facilitate the IM ossification. The proper hypoxic microenvironment and the MV primed osteogenic conditions integrate the EC and IM ossification to promote the regeneration of bone defects. Our previous study had shown that the MV did not influence the proliferation of the BMSCs [36], and the evaluation of the adhesion and proliferation of BMSCs on PH/GOG composites showed that the PH15 had the best biocompatibility. We selected the PH, PH5M, PH15M, and PH30M to conduct further research to analyze the bio-functions of the biomimetic procallus mixed with MV/GOG.

Due to the effect of MV on priming the progenitors, we firstly tested the osteogenic effect of the biomimetic procallus on the BMSCs. The ALP staining of the BMSCs seeded on the biomimetic procallus at 7 d (Fig. 5c) showed that the PH15M had the best osteogenic effect. The composites with less or more MV/GOG showed a decreased impact on osteogenesis in ALP staining. Additionally, the light view of BMSCs on the composites at 21 d (Figure S3e, Supporting Information) showed similar results with ALP staining, more extensive cellular aggregation, and mineralized node. The decreased osteoinductive effect of PH30M may be resulted from the oxidative stress injury on BMSCs due to the ROS aroused from a large amount of MV/GOG. A balance between the oxidative damage of MV/GOG and the primed osteoinductive effect from MV was needed to attain to elicit a potential impact on osteogenesis. Runx2 immunofluorescent staining at 7 d (Fig. 5d) and Col1 at 21 d (Fig. 5e) for BMSCs seeded on the composites with different MV/GOG ratios showed the results consistent with the ALP staining. The expression of Runx2 was increased significantly at 7 d in PH15M compared to other composites, which indicated the best osteogenic effect at the early stage. Col1 also presented the most extensive nodules of mineralization due to the better osteogenic effect of PH15M at the later stage of osteogenic differentiation. The osteogenic effect of the PH15 without MV containing the same amount of GOG with PH15M was also tested to illustrate the osteogenic effect of the composite just incorporating GOG. The result (Figure S3f, g, Supporting Information) showed that the composite only with GOG also had a weak osteogenic effect due to GOG's property. Quantitative real-time PCR was conducted to investigate the osteogenic differentiation of BMSCs cultured on different composites (Fig. 5f). Compared with the pure gelatin group (PH), the gene expressions involved in osteoblastic differentiation such as Runx2, ALP, Col1 and OCN were upregulated

significantly in PH5M, and PH15M was attributed to the outstanding osteoinductive effect of the composites. However, high concentrations of MV/GOG in the PH30M group displayed a negative impact on the regulation of the osteogenic-related genes compared with the PH15M, which showed that a balance between the osteoinductive effect of MV and the side-effect of MV/GOG needed to be attained to elicit an ideal osteogenic impact. The best outcome of PH15M on the osteoblast related gene expression was attributed to the controlled release of MV and the proper microstructure of the composite due to the mixture of MV/GOG. The best osteogenic effect of PH15M at all the time points verified the best balance to exert its bio-functions.

Considering the hypoxia condition caused by GOG in the biomimetic procallus, the circular distribution pattern of BMSCs in the results of the ALP staining, Runx2 and Col1 immunofluorescence staining implied the angiogenic effect of the biomimetic procallus. For amplifying the distribution pattern of the BMSCs to clarify the angiogenic effect of the biomimetic procallus, we seeded BMSCs on the composites with a less cell density to analyze the angiogenic differentiation of the BMSCs. The impact of the biomimetic procallus on the angiogenic differentiation of BMSCs was investigated through staining the β-actin and endothelial marker CD31 (Fig. 5g). Meanwhile, the circular pattern of the BMSCs was also quantified in terms of the total capillary branch lengths, the number of circles, and the number of nude points (Fig. 5h). The schematic illustration (Figure S3h, Supporting information) showed the branch, loop, and nude defined by the NIH ImageJ 1.45 software automatically. BMSCs cultured on the PH15M composite could form the capillary-like tubes with the expression of CD31 at 7 d. Compared with PH, the formation of vascular tubes in PH15M was more shaped in a capillary-like network. Meanwhile, the total capillary branch length, the number of circles, and the number of nude points per field also increased significantly (p < 0.05). However, the PH30M composite inhibited tube formation of BMSCs. It was worthwhile pointing out that the marker of the endothelial cell CD31 was expressed in the cells that formed the capillary-like circles, which verified that the composite could induce the angiogenic differentiation of the BMSCs. To prove the angiogenic effect of the composite resulted from the GOG mixed in the hydrogel, the PH/MV composite that had the same amount MV as PH15M composite but without GOG was constructed to compare the angiogenic effect of it with PH15M composite. The result (Figure S3i, Supporting information) proved that the composite without GOG just containing MV did not represent the same angiogenic effect with the PH15M, and the performance of it was only equivalent to the PH without MV/GOG. The gene expressions of endothelial markers, Ang1, VEGF, vWF, and CD31 were also assayed by qRT-PCR at 7d to illustrate the angiogenic differentiation of BMSCs after cultured on the different composites (Fig. 5i). Compared with the control group (PH), the composite of PH15M upregulated the expression of Ang1, VEGF, vWF, and CD31 of BMSCs significantly (p < 0.05). With further increase of MV/GOG, the expression of endothelial markers was decreased compared to the PH15M. All the results showed that the PH15M also showed the best angiogenic effect except for the osteoinductive fact. The proper ratio of GOG in the biomimetic procallus could elicit an appropriate condition of hypoxia for angiogenesis. Meanwhile, the MV delivered by GOG also primed the osteogenesis of the BMSCs in combination with the stimulus of the bioactive signals in the procallus.

To verify the best ratio of MV/GOG and the specific bioactive signals in the biomimetic procallus for eliciting its bio-functions, the Western blot analysis of the related protein expression was conducted to replenish the schematic illustration of the biomimetic procallus with bioactive signals system (Fig. 3g). The results of Western blot (Fig. 5j) showed that the phosphorylation of Erk1/2 and AKT pathway was gradually enhanced at 12 h with the increased amounts of MV/GOG in the composites except for the decreased expression in PH30M, meanwhile the expression of Mcl1 had the same pattern. The expressions of VEGF and Runx2 at 7 d (Fig. 5k) were also increased with the increased MV/GOG in the composites except for the decreased expression in
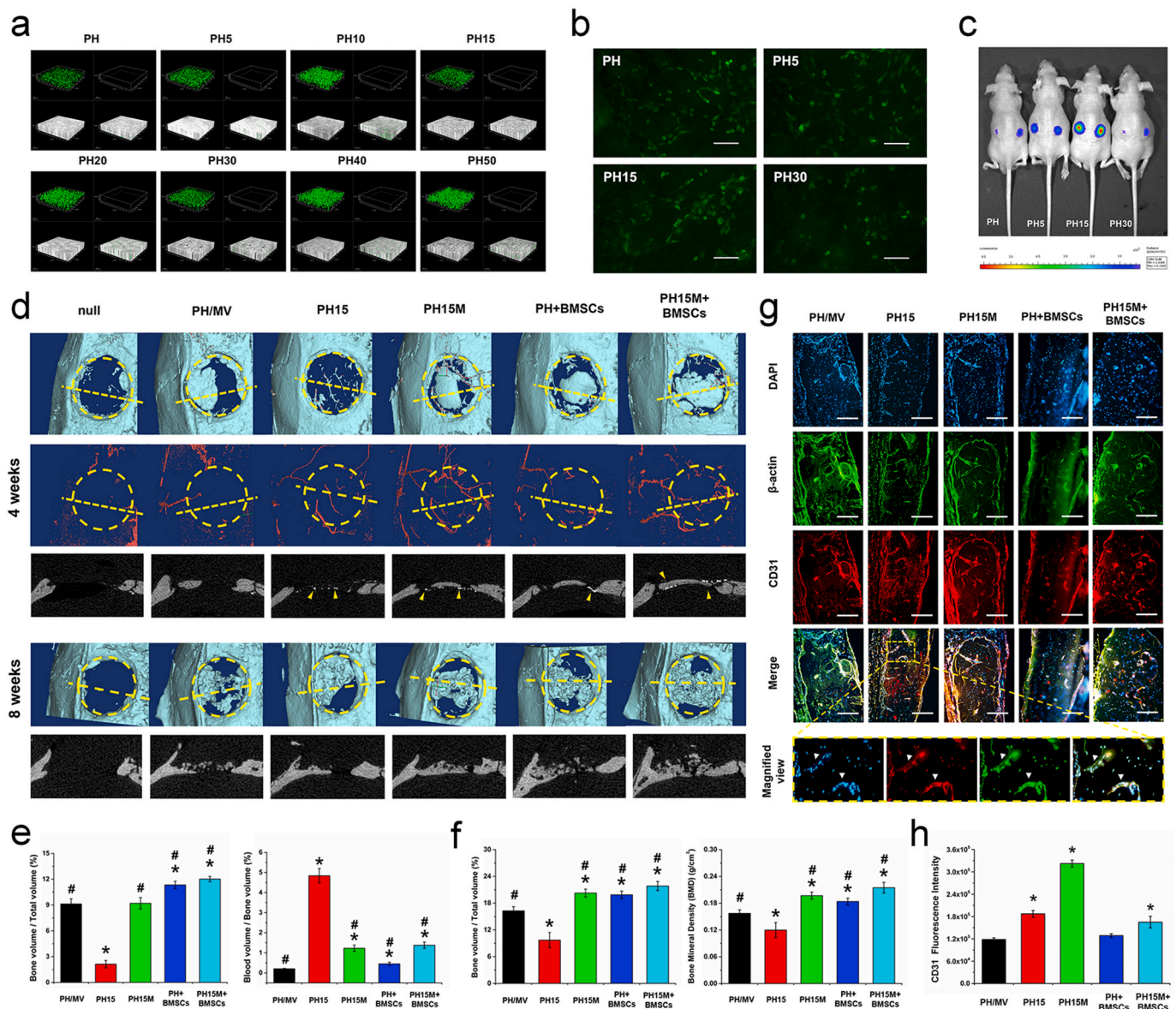
Fig. 6. The repairment of rat calvarial defect by the biomimetic procallus. a) The live/dead of the BMSCs seeded in the PH/GOG composites. b) The NO synthesis in the BMSCs mixed in the PH/GOG composites. Bar: 250 μm. c) Fluorescence imaging showed the viability of the Lenti-luciferase transfected BMSCs mixed in PH/GOG composites after 7 d. d) The μCT analysis of the bone defect at 4 weeks and 8 weeks. The yellow dotted lines showed the location of the section view below the reconstructed 3D views, the yellow arrow heads indicate the new blood vessel perfused with the contrast media which has the larger radiodensity compared with the bone. e) The quantitative analysis of the new bone and the blood vessels in the VOI at 4 weeks. *: $p < 0.05$ versus PH/MV; #: $p < 0.05$ versus PH15. f) The quantitative analysis of the new bone and Bone Mineral Density in the VOI at 8 weeks. *: $p < 0.05$ versus PH/MV; #: $p < 0.05$ versus PH15. g) Immunofluorescence stain of the endothelial marker CD31 in the sections. The arrow heads in the magnified view show the new blood vessel in the new bone. Bar: 100 μm. h) The statistics of CD31 immunofluorescence intensity showed increased signals in the groups with GOG. *: $p < 0.05$ versus PH/MV. (For interpretation of the references to color in this figure legend, the reader is referred to the Web version of this article.)

PH30M, which clarified the bi-differentiation of the BMSCs. Additionally, the level of OCN and OPN at 21 d (Figure 5l) was also upregulated, illustrating the high-grade mineralization in the later stage, consistent with the earlier time point in the experiments. These results verified that the proper mechanical properties and hypoxia condition in PH15M could activate the subsequent bioactive signals to elicit its bio-functions, such as promoting cell adhesion, proliferation, differentiation, and resisting the apoptosis of the cell. For proving the correlation between the Erk1/2 pathway and the bi-differentiation of the BMSCs, we blocked the Erk1/2 pathway to test the change of the expression of the related proteins in the bi-differentiation of BMSCs. The cell treated with PD98059 (CST, Beverly, MA, USA), an inhibitor of the Erk1/2 signal pathway, showed decreased osteogenic and angiogenic proteins in the

PH15M composite (Figure 5m). Because the amount of MV in PH15M + PD98059 was the same as the PH15M, the reduced osteogenic property of the composite may result from the block of the Erk1/2 signal pathway. Therefore, the activation of Erk1/2 signal pathway by GOG can promote the osteogenic and angiogenic effects of the PH/MV/GOG composite. All the quantitative protein analysis results showed that the PH15M composite had the best impact of exerting the bioactive signals to promote osteogenic and angiogenic differentiation of the BMSCs. The integrin-mediated sequent signal transduction and the proper ROS level could activate the Erk1/2 and AKT signal pathway to improve the osteogenesis and angiogenesis. In the biomimetic procallus, GOG played a crucial role in promoting cell adhesion and constructing a hypoxia microenvironment to bio-mimic the procallus, which owns the porous

Fig. 7. The histological evaluation of the repairment by biomimetic procallus. a) The histological analysis of the repairment of the defect with different implant. Bar: 1 mm. b) Sequential fluorescent labeling of the new bone formation by Alizarin Red S (AL), Calcein (CA) and Tetracyclin Hydrochloride (TE). Bar: 200 μm. c) The quantitative analysis of the Masson stain of the new bone formed in the defect. *: $p < 0.05$ versus PH/MV; #: $p < 0.05$ versus PH15M. d) Quantitative analysis of the area of new bone formation labeled by AL, CA and TE. *: $p < 0.05$ versus PH/MV; #: $p < 0.05$ versus PH15M. e) Schematic illustration showed that the PH15 composite mimicked the procallus with the proper structure and promised the bio-inspired natures, meanwhile MV/GOG reinforced the bioactive signals system to exert the osteogenic and angiogenic properties of the biomimetic procallus. (For interpretation of the references to color in this figure legend, the reader is referred to the Web version of this article.)

structure and bioactive signals suitable for the reparative phase of the bone healing process.

In summary, the GOG plays a crucial role in regulating the biomimetic procallus in all aspects, including cell adhesion, proliferation, differentiation, and survival. Meanwhile, it also deliveries and modulates the bioactive signals system to construct the semi-autonomous procallus. With the bi-differentiation of the progenitors in the procallus, the angiogenesis caused by the initial hypoxia gradually relieves the hypoxic tension to promote further osteogenesis along with the MV priming condition, which mimics the whole stage from the initial inflammatory phase to subsequent reparative and remodeling phases illustrating the path-dependence nature of the developmental engineering. The stable microenvironment constructed by the biomimetic materials, progenitors and bioactive signals system promises the Robustness nature of the developmental engineering, which comes naturally with the progress of the dynamic procallus.

3.5. Evaluations of critical calvarial defect repair and new blood vessel formation in vivo

To further analyze the bio-functions of the biomimetic procallus *in vivo*, we firstly tested the biocompatibility of the procallus on the BMSCs mixed in it for bone repair. The result of live/dead staining (Fig. 6a) presented that the composites with different ratios of GOG had no cytotoxicity to the cells mixed in the composites at 1 d. The NO immunofluorescent staining (Fig. 6b) showed that the NO synthesis in BMSCs had the best activity in the PH15, consistent with the pre-described results about the proper mechanical properties and hypoxia condition in PH15. For evaluating the viability and proliferation of the BMSCs in the procallus, Lenti-luciferase transfected BMSCs were mixed with different PH/GOG composites, and the mixture was subcutaneously transplanted in nude mice to test the viability of BMSCs in various composites. The bioluminescent imaging results *in vivo* (Fig. 6c) showed the best sustainability of BMSCs in PH15 composite. Compared with the PH15 group, the more GOG mixed in the PH30 composite was not suitable for the survival of the mixed BMSCs. The good viability of BMSCs in PH15 maybe resulted from better angiogenesis and the proper mechanical properties, which promised an excellent ECM microenvironment for the survival and proliferation of the BMSCs.

In the repair of the rat critical calvarial defect, we evaluated the different implants' different groups, including the PH15M implant, the PH15 implant without MV, the PH/MV implant with the same dose of MV, but no GOG, PH + BMSCs and the PH15M + BMSCs implant. The PH15 mimicked the inflammatory stage of bone healing without the MV primed osteogenesis and the implanted BMSCs, which just repaired the bone defect depending on the recruited progenitor from the host tissue for the EC ossification. The PH/MV without GOG didn't show the hypoxia condition caused by GOG and just contained the osteoinductive factor MV, which lost the better angiogenesis but had the direct osteogenesis primed by MV for IM ossification. PH15M owned both the better angiogenesis caused by hypoxia and the direct osteogenesis primed by MV, which combined the EC and IM ossifications for the repair of the bone defect. Mixed with the BMSCs, the PH + BMSCs showed the bone repair function of pure hydrogel combining with stem cell. With further addition of MV loaded GOG in composite, the PH15M + BMSCs implant showed the best potential of the angiogenesis and osteogenesis for rapid bone repair. The collected samples of rat critical calvarial defects at 4 and 8 weeks were scanned by μCT system to evaluate the effect of different implants on the repairment of the critical-sized defects *in vivo* (Fig. 6d). At 4 weeks, the 3D μCT images revealed that the newly formed bone tissue could be barely observed at the defect site of the new and PH15, while a small amount of newly formed bone could be found in the circumference of the PH/MV. It showed that the MV primed IM ossification could promote the more bone regeneration compared with the GOG induced EC ossification in the early phase of bone repair. The undetected bone formation in the PH15 may be resulted from the

chondrogenesis process due to the undirect osteogenesis of the EC ossification. For the PH15M, PH + BMSCs and PH15M + BMSCs, the newly formed bone occurred at the center of the defect site, which implied that the combination of EC and IM ossification for bone repair could promote the rapid bone regeneration. Furthermore, the blood vessels that were reconstructed from the perfusion of barium sulfate suspension significantly showed more blood vessels both around and inside the implants with the mix of GOG. This result demonstrated that the mixed GOG could induce angiogenesis of the repairment in the bone defect. The quantitative analysis of the bone regeneration (Fig. 6e) showed that the groups of the PH/MV, PH15M, PH + BMSCs and PH15M + BMSCs demonstrated significantly higher values of BV/TV than the PH15 at 4 weeks (p < 0.05). The ratio of blood volume to bone volume in PH15 was the largest compared to other groups (p < 0.05). It showed that the IM ossification facilitated bone formation in the short term without the intermediate chondrogenesis and angiogenesis in EC ossification. The trabecular bone parameters and the SMI also showed the difference between the groups at 4 weeks (Figure S3j, Supporting information). The Tb. N showed the same pattern with the BV/TV. Besides, the Tb. Sp of the PH15 was also the largest due to the least amount of bone formation (p < 0.05). The Tb. Th and SMI of these composites did not show a significant difference at 4 weeks.

At 8 weeks, the results of μCT in 3D images (Fig. 6d) showed a similar effect of the PH/MV and PH15. Both of the groups showed regeneration of bone tissue derived from the peripheral of the bone defect. However, the defect of PH15 appeared to be more repaired due to the better angiogenesis compared with the PH/MV, which resulted from the effect of GOG in PH15. The impact of the PH15M + BMSCs on bone defect repairment was slightly better than the PH15M and PH + BMSCs, in which there was more bone bridge formation to repair the integrity at 8 weeks. These results revealed that the faster rate of the new bone regeneration in the center of the defect has resulted from better angiogenesis and MV-primed osteogenesis in the early repair stage. Meanwhile, the progenitors mixed in the implant could favor the repair of the bone defects in PH + BMSCs and PH15M + BMSCs. Moreover, the quantitative analysis of the newly formed bone (Fig. 6f) also supports the effect of angiogenesis and MV-primed osteogenesis of the progenitors on bone repair. The PH15M, PH + BMSCs and PH15M + BMSCs showed significantly higher BMD, BV/TV than the PH/MV, and PH15 (p < 0.05). The parameters concerning the trabecular bone and the SMI presented the structure difference between the groups at 8 weeks (Figure S3k, Supporting information). The Tb. N values also showed the same pattern to BV/TV. The structure model index (the value is from 0 to 3) was used to reflect the bone structure, the trabecular bone was a rod-like structure with the value of SMI nearly to 3, and the cortical bone with a plate-like structure had a value of SMI approximate to 0. The smaller SMI and Tb. Sp in the PH15M, PH + BMSCs and PH15M + BMSCs showed the better construction of the newly formed bone. The difference between the values of Tb. Th in these groups was not significant. By observing the new bone's angiogenesis, especially in the composites with GOG, we could see that many new blood vessels appeared inside or around the new bone, accompanying the appearance of the endotheliocytes stained by CD31 (Fig. 6g). Through the observation on the new bone at high power magnification at 8 weeks, some apparent new blood vessels could be identified inside the new bone with an expression of the endothelial marker CD31 in the PH15. Besides, the quantitative analysis of the CD31 fluorescence intensity also showed the apparent better angiogenesis of the new bone formation in the composites with GOG at 8 weeks (Fig. 6h). These showed that the GOG induced hypoxia condition could promote the angiogenesis of the EC ossification and provide more nutrition for the subsequent bone formation.

The histological analysis of the samples at 8 weeks further supported the μCT study of the defect. The bones defect sections were prepared longitudinally according to the long axis of the skull and were stained by HE and Masson to present the repair of bone defect in different groups

(Fig. 7a). The blank without implant did not form bone instead of soft tissue residues at 8 weeks. The separated blocky new bone could be found in the PH/MV, which illustrated the structural pattern of IM ossified bone. As for the PH15, due to GOG mixed in the composite, the better angiogenesis of the defect also promoted the new bone repair. The bone formation through EC ossification in PH15 illustrated a smaller amount of new bone compared with PH/MV at 8 weeks. When combining the effect of MV and GOG, the PH15M showed better repair of the defect with more massive new bone. The repaired bone was composed of the mature trabecular bone meshwork and the new blood vessels that formed around and inside the new bone. It could result from the combination of EC and IM ossifications induced by GOG and MV, respectively. The PH + BMSCs group showed the effect of stem cell on bone repair and the gelatin hydrogel containing BMSCs showed a good defect repair. Combining with MV/GOG mixture, the group of the PH15M + BMSCs showed a more significant and thicker new bone formation in the center of the bone defect, which illustrated the promotive effect of the progenitors on the bone repair. The tricolor fluorescent labeling analysis was used to present the difference of the new bone formation between the different samples after implanting the composites 8 weeks, in which the Alizarin Red S (AL), Calcein (CA), and Tetracyclin Hydrochloride (TE) were injected intraperitoneally to label the bone formation and mineralization at 2, 4, and 6 weeks correspondingly (Fig. 7b). Besides, the quantitative analysis of the bone formation in Masson stain (Fig. 7c) also illustrated the larger ratio of mature bone to the osteoid matrix in PH/MV, PH + BMSCs and PH15M + BMSCs compared with PH15 and PH15M, which showed the osteogenic effect of MV and BMSCs, respectively. The quantitative analysis of the fluorochrome stained bone (Fig. 7d) demonstrated that the percentage of AL labeling (Red) in the composite with GOG or MV alone was similar to each other at 2 weeks, and the combining of GOG and MV showed a rapid regeneration of the new bone with a larger ratio of stained bone in PH15M and PH15M + BMSCs ($p < 0.05$). Meanwhile, the BMSCs in PH + BMSCs also favored a rapid new bone formation compared with PH/MV and PH15. At 4 weeks, the PH15M + BMSCs had the best effect of regeneration with the most significant area and more comprehensive CA label. A larger percentage of CA labeling (Green) was also observed in the composites with MV/GOG compared with the groups just containing an element of MV/GOG. Meanwhile, PH15M + BMSCs also had a significant increase of new bone than that PH15M without cell. The PH + BMSCs also showed lager new bone formation area than PH/MV and PH15, which illustrated the promotive effect of BMSCs on bone defect repair. After 6 weeks, the amount of TE labeling (Yellow) in the PH15M, PH + BMSCs and PH15M + BMSCs was higher than in the PH/MV and PH15 groups.

All the results showed that the PH15M + BMSCs implant had the best bone repair effect, which resulted from the combination of EC and IM ossifications. The GOG caused hypoxia condition induced angiogenesis and provided more nutrition for the EC ossification. Meanwhile, the MV primed IM ossification through the direct osteogenesis, which promotes the biomimetic procallus to produce more newly-formed bone. The implant could mimic the whole process from the initial inflammatory stage to the reparative stage in bone healing, which promises rapid and excellent repair performance.

4. Conclusion

In this study, GOG, as the combination of GO and gelatin, showed the double-phase character to elicit its bio-functions, including excellent biocompatibility for regulating progenitor differentiation, nanofiller for the photo-crosslinked hydrogel, and nanocarrier for delivery the bioactive signals. We presented that there was no side influence on cell mitosis and autophagy during BMSCs uptake of GOG, which promised its excellent biocompatibility as a nanocarrier. As the filler, GOG could modify the mechanical properties of gelatin hydrogel to promote the adhesion, proliferation, and differentiation of the BMSCs. The gelatin

immobilized on GOG makes it act as MV's carrier for priming the osteogenesis of BMSCs. With the realm of developmentally engineering, the biomimetic procallus was certified not only to be the ideal bioactive materials that mimic the relevant ECM composition but also to the bio-functional materials that mimic the developmental process eliciting the bioactive signals system (Fig. 7e). Because the over-dose of GOG in the biomimetic procallus intrigues the ROS damage, a balance between the delivered MV and the ROS damage needs be attained to construct the proper composites that own both osteogenic and angiogenic effects. With the bi-differentiation of the progenitors in the procallus, the angiogenesis caused by the initial hypoxia gradually relieves the hypoxic tension to promote further osteogenesis along with the MV priming condition. The biomimetic procallus mimics the whole stage from the initial inflammatory phase to subsequent reparative and remodeling phases, showing the path-dependence nature of developmental engineering. The biomimetic procallus also enhanced both the EC and IM ossification for rapid bone repair. The osteoinductive, angiogenic, and proper mechanical properties of the biomimetic procallus contribute to the robustness and semi-autonomy nature of developmental engineering. In all the processes, the biocompatible GOG plays a pivotal role in regulating the biomimetic procallus. It is the first time to report the application of GOG in developmental engineering, and we also construct a promised biomimetic procallus for rapid bone repair.

Credit author statement

Delong Jiao and Ao Zheng: Conceptualization, Data curation, Investigation, Methodology, Writing original draft. Wenjun She: Methodology, Formal analysis. Yang Liu: Formal analysis, Data curation. Xiangkai Zhang: Methodology, Validation. Xiao Wang: Resources, Validation. Jiannan Wu: Validation, Data curation. Kaige Lv, Lingyan Cao and Xinquan Jiang: Conceptualization, Funding acquisition, Project administration, Writing review & editing, Supervision.

Declaration of competing interest

The authors declare no conflict of interest.

Acknowledgments

Appendix A. Supplementary data

Supplementary data to this article can be found online at https://doi.org/10.1016/j.bioactmat.2020.12.003.

References

[1] W. Niu, W. Guo, S. Han, Y. Zhu, S. Liu, Q. Guo, Cell-based strategies for meniscus tissue engineering, Stem Cell. Int. 2016 (2016) 4717184.

[2] P. Lenas, M. Moos, F.P. Luyten, Developmental engineering: a new paradigm for the design and manufacturing of cell-based products. Part I: from three-dimensional cell growth to biomimetics of in vivo development, Tissue Eng. B Rev. 15 (4) (2009) 381.

[3] P. Lenas, M. Moos, F.P. Luyten, Developmental engineering: a new paradigm for the design and manufacturing of cell-based products. Part II: from genes to networks: tissue engineering from the viewpoint of systems biology and network science, Tissue Eng. B Rev. 15 (4) (2009) 395–422.

[4] E.J. Mackie, Y.A. Ahmed, L. Tatarczuch, K.S. Chen, M. Mirams, Endochondral ossification: how cartilage is converted into bone in the developing skeleton, Int. J. Biochem. Cell Biol. 40 (1) (2008) 46–62.

[5] A. Schindeler, M.M. Mcdonald, P. Bokko, D.G. Little, Bone remodeling during fracture repair: the cellular picture, Semin. Cell Dev. Biol. 19 (5) (2008) 459–466.

[6] M. Manav, S.B. Katharina, G.N. Duda, D.J. Mooney, Biomaterial delivery of morphogens to mimic the natural healing cascade in bone, Adv. Drug Deliv. Rev. 64 (12) (2012) 1257–1276.

[7] L.C. Gerstenfeld, D.M. Cullinane, G.L. Barnes, D.T. Graves, T.A. Einhorn, Fracture healing as a post-natal developmental process: molecular, spatial, and temporal aspects of its regulation, J. Cell. Biochem. 88 (5) (2003) 873–884.

[8] G. Du, L. Nie, G. Gao, Y. Sun, R. Hou, H. Zhang, T. Chen, J. Fu, Tough and biocompatible hydrogels based on in situ interpenetrating networks of dithiol-connected graphene oxide and poly(vinyl alcohol), ACS applied materials & interfaces [C@d04aab[C@e70a98) (2015) 3003–3008.

[9] W. Kong, D. Huang, G. Xu, J. Ren, C. Liu, L. Zhao, R. Sun, Graphene oxide/polyacrylamide/aluminum ion cross-linked carboxymethyl hemicellulose nanocomposite hydrogels with very tough and elastic properties, Chem. Asian J. 11 (11) (2016) 1697–1704.

[10] C. Pan, L. Liu, G. Gai, Recent progress of graphene-containing polymer hydrogels: preparations, properties, and applications, Macromol. Mater. Eng. 302 (10) (2017) 1700184.

[11] Y. Wang, C. Song, X. Yu, L. Liu, Y. Han, J. Chen, J. Fu, Thermo-responsive hydrogels with tunable transition temperature crosslinked by multifunctional graphene oxide nanosheets, Compos. Sci. Technol. 151 (2017) 139–146.

[12] N. Dubey, R. Bentini, I. Islam, T. Cao, A.N. Castro, V. Rosa, Graphene: a versatile carbon-based material for bone tissue engineering, Stem Cell. Int. 2015 (2015) 804213.

[13] L. Zhang, J. Xia, Q. Zhao, L. Liu, Z. Zhang, Functional graphene oxide as a nanocarrier for controlled loading and targeted delivery of mixed anticancer drugs, Small 6 (4) (2010) 537–544.

[14] J. Linares, M.C. Matesanz, M. Vila, M.J. Feito, G. Gonçalves, M. Valletregí, P. A. Marques, M.T. Portolés, Endocytic mechanisms of graphene oxide nanosheets in osteoblasts, hepatocytes and macrophages, ACS Appl. Mater. Interfaces 6 (16) (2014) 13697.

[15] T.R. Nayak, A. Henrik, V.S. Makam, K. Clement, B. Sukang, X. Xiangfan, P.L.R. Ee, A. Jong-Hyun, H. Byung Hee, P. Giorgia, Graphene for controlled and accelerated osteogenic differentiation of human mesenchymal stem cells, ACS Nano 5 (6) (2011) 4670–4678.

[16] O. Akhavan, E. Ghaderi, M. Shahsavar, Graphene nanogrids for selective and fast osteogenic differentiation of human mesenchymal stem cells, Carbon 59 (7) (2013) 200–211.

[17] S.W. Crowder, P. Dhiraj, R. Rutwik, D.A. Balikov, B. Hojae, K.I. Bolotin, S. Hak-Joon, Three-dimensional graphene foams promote osteogenic differentiation of human mesenchymal stem cells, Nanoscale 5 (10) (2013) 4171–4176.

[18] S. Mukherjee, P. Sriram, A.K. Barui, S.K. Nethi, V. Veeriah, S. Chatterjee, K. I. Suresh, C.R. Patra, Graphene oxides show angiogenic properties, Advanced Healthcare Materials 4 (11) (2015) 1722–1732.

[19] K. Liu, J.-J. Zhang, F.-F. Cheng, T.-T. Zheng, C. Wang, J.-J. Zhu, Green and facile synthesis of highly biocompatible graphene nanosheets and its application for cellular imaging and drug delivery, J. Mater. Chem. 21 (32) (2011) 12034.

[20] Y. Wang, J. Hao, Z. Huang, G. Zheng, C. Shen, Flexible electrically resistive-type strain sensors based on reduced graphene oxide-decorated electrospun polymer fibrous mats for human motion monitoring, Carbon 126 (2017).

[21] S. Asha, A.N. Ananth, S.P. Jose, M.A.J. Rajan, Reduced Graphene Oxide Aerogel Networks with Soft Interfacial Template for Applications in Bone Tissue Regeneration, Applied Nanoence, 2018.

[22] J.W. A, Y.C. B, L.C. A, T.Z. A, K.Y. A, C.J. C, H.W. C, M.Z. D, C.F. B, X.M. A, In vitro and in vivo studies of electroactive reduced graphene oxide-modified nanofiber scaffolds for peripheral nerve regeneration, Acta Biomater. 84 (2019) 98–113.

[23] J.A. Hunt, R. Chen, T.V. Veen, N. Bryan, Hydrogels for tissue engineering and regenerative medicine, J. Mater. Chem. B 2 (33) (2014) 5319–5338.

[24] B. Xin, M. Gao, S. Syed, J. Zhuang, X. Xu, X.Q. Zhang, Bioactive hydrogels for bone regeneration, Bioactive Materials 3 (4) (2018) 401–417.

[25] S.J. Bryant, K.S. Anseth, Hydrogel properties influence ECM production by chondrocytes photoencapsulated in poly(ethylene glycol) hydrogels, J. Biomed. Mater. Res. 59 (1) (2010).

[26] R.E. Kania, A. Meunier, M. Hamadouche, L. Sedel, H. Petite, Addition of fibrin sealant to ceramic promotes bone repair: long-term study in rabbit femoral defect model, J. Biomed. Mater. Res. 43 (1) (1998) 38.

[27] J.J. Zhang, M.M. Gu, T.T. Zheng, J.J. Zhu, Synthesis of gelatin-stabilized gold nanoparticles and assembly of carboxylic single-walled carbon nanotubes/Au composites for cytosensing and drug uptake, Anal. Chem. 81 (16) (2009) 6641–6648.

[28] D.A. Fancy, T. Kodadek, Chemistry for the analysis of protein-protein interactions: rapid and efficient cross-linking triggered by long wavelength light, Proc. Natl. Acad. Sci. U. S. A. 96 (11) (1999) 6020–6024.

[29] C.M. Elvin, A.G. Carr, M.G. Huson, J.M. Maxwell, R.D. Pearson, T. Vuocolo, N. E. Liyou, D.C. Wong, D.J. Merritt, N.E. Dixon, Synthesis and properties of crosslinked recombinant pro-resilin, Nature 437 (7061) (2005) 999–1002.

[30] C.M. Elvin, A.G. Brownlee, M.G. Huson, T.A. Tebb, M. Kim, R.E. Lyons, T. Vuocolo, N.E. Liyou, T.C. Hughes, J.A. Ramshaw, J.A. Werkmeister, The development of photochemically crosslinked native fibrinogen as a rapidly formed and mechanically strong surgical tissue sealant, Biomaterials 30 (11) (2009) 2059–2065.

[31] C.M. Elvin, S.J. Danon, A.G. Brownlee, J.F. White, M. Hickey, N.E. Liyou, G. A. Edwards, J.A. Ramshaw, J.A. Werkmeister, Evaluation of photo-crosslinked fibrinogen as a rapid and strong tissue adhesive, J. Biomed. Mater. Res. 93 (2) (2010) 687–695.

[32] C.M. Elvin, T. Vuocolo, A.G. Brownlee, L. Sando, M.G. Huson, N.E. Liyou, P. R. Stockwell, R.E. Lyons, M. Kim, G.A. Edwards, G. Johnson, G.A. McFarland, J.

A. Ramshaw, J.A. Werkmeister, A highly elastic tissue sealant based on photopolymerised gelatin, Biomaterials 31 (32) (2010) 8323–8331.

[33] A.T. Neffe, A. Zaupa, B.F. Pierce, D. Hofmann, A. Lendlein, Knowledge-based tailoring of gelatin-based materials by functionalization with tyrosine-derived groups, Macromol. Rapid Commun. 31 (17) (2010) 1534–1539.

[34] H. Borginon, L.W. Ketellapper, D. Rouck, A comparison of different methods for the determination of the reducing properties of photographic gelatin *, Journal of Photographic ence 28 (3) (1980) 111–118.

[35] H. Kobayashi, T. Yamaga, Y. Okawa, T. Ohno, Studies on the reducing properties of gelatin - kinetics of the reaction with copper (II) bis(bipyridine), Journal of Photographic ence 48 (3) (2000) 141–145.

[36] D. Jiao, L. Cao, Y. Liu, J. Wu, A. Zheng, X. Jiang, Synergistic osteogenesis of biocompatible reduced graphene oxide with methyl vanillate in BMSCs, ACS Biomater. Sci. Eng. 5 (4) (2019) 1920–1936.

[37] Y. Wu, L. Cao, L. Xia, Q. Wu, J. Wang, X. Wang, L. Xu, Y. Zhou, Y. Xu, X. Jiang, Evaluation of osteogenesis and angiogenesis of icariin in local controlled release and systemic delivery for calvarial defect in ovariectomized rats, Sci. Rep. 7 (1) (2017) 5077.

[38] J.G. Chen, R. Hinesley, S.A. Kempson, Dual action of colchicine on hypertonic activation of system A amino acid transport in vascular smooth muscle cells, Life Sci. 61 (1) (1997) 29–37.

[39] V. Bandmann, J.D. Müller, T. Köhler, U. Homann, Uptake of fluorescent nano beads into BY2-cells involves clathrin-dependent and clathrin-independent endocytosis, FEBS Lett. 586 (20) (2012) 3626–3632.

[40] T. Bhowmick, E. Berk, X. Cui, V.R. Muzykantov, S. Muro, Effect of flow on endothelial endocytosis of nanocarriers targeted to ICAM-1, J. Contr. Release 157 (3) (2012) 485–492.

[41] W.L. Schulz, A.K. Haj, L.A. Schiff, Reovirus uses multiple endocytic pathways for cell entry, J. Virol. 86 (23) (2012) 12665–12675.

[42] Kylie M. Wagstaff, H. Sivakumaran, Steven M. Heaton, D. Harrich, David A. Jans, Ivermectin is a specific inhibitor of importin α/β-mediated nuclear import able to inhibit replication of HIV-1 and dengue virus, Biochem. J. 443 (3) (2012) 851–856.

[43] W. Zhang, C. Zhu, D. Ye, L. Xu, X. Zhang, Q. Wu, X. Zhang, D.L. Kaplan, X. Jiang, Porous silk scaffolds for delivery of growth factors and stem cells to enhance bone regeneration, PLoS One 9 (7) (2014), e102371.

[44] L. Cao, J. Wang, J. Hou, W. Xing, C. Liu, Vascularization and bone regeneration in a critical sized defect using 2-N,6-O-sulfated chitosan nanoparticles incorporating BMP-2, Biomaterials 35 (2) (2014) 684–698.

[45] W.J. Zhang, G.C. Wang, Y. Liu, X.B. Zhao, D.H. Zou, C. Zhu, Y.Q. Jin, Q.F. Huang, J. Sun, X.Y. Liu, X.Q. Jiang, H. Zreiqat, The synergistic effect of hierarchical micro/nano-topography and bioactive ions for enhanced osseointegration, Biomaterials 34 (13) (2013) 3184–3195.

[46] S.K. Lam, Y.C. Tse, D.G. Robinson, L. Jiang, Tracking down the elusive early endosome, Trends Plant Sci. 12 (11) (2007) 497–505.

[47] B. Vanhaesebroeck, S.J. Leevers, G. Panayotou, M.D. Waterfield, Phosphoinositide 3-kinases: a conserved family of signal transducers, Trends Biochem. Sci. 22 (7) (1997) 267–272.

[48] M.C. Alliegro, Coiled body heterogeneity induced by G(1) arrest with amiloride + bumetanide, Exp. Cell Res. 279 (1) (2002) 111–117.

[49] D. Staněk, K.M. Neugebauer, The Cajal body: a meeting place for spliceosomal snRNPs in the nuclear maze, Chromosoma 115 (5) (2006) 343–354.

[50] O. Pontes, C.S. Pikaard, siRNA and miRNA processing: new functions for Cajal bodies, Curr. Opin. Genet. Dev. 18 (2) (2008) 197–203.

[51] A. Sudarshan, D.A. Cheresh, Emerging role of micro-RNAs in the regulation of angiogenesis, Genes & Cancer 2 (12) (2011) 1134.

[52] C. Dou, N. Ding, F. Luo, T. Hou, Z. Cao, Y. Bai, C. Liu, J. Xu, S. Dong, Graphene-based MicroRNA transfection blocks preosteoclast fusion to increase bone formation and vascularization, Advanced Science 5 (2) (2018) 1870009.

[53] M. Kalbacova, A. Broz, J. Kong, M. Kalbac, Graphene substrates promote adherence of human osteoblasts and mesenchymal stromal cells, Carbon 48 (15) (2010) 4323–4329.

[54] S. A, P. Ls, C. P, M. D, N. S, R. Cn, K. M, Differential nano-bio interactions and toxicity effects of pristine versus functionalized graphene, Nanoscale 3 (6) (2011) 2461–2464.

[55] Y. Li, H. Yuan, d.B.A. Von, M. Creighton, R.H. Hurt, A.B. Kane, H. Gao, Graphene microsheets enter cells through spontaneous membrane penetration at edge asperities and corner sites, Proc. Natl. Acad. Sci. U.S.A. 110 (30) (2013) 12295–12300.

[56] T. Sakai, T. Matsunaga, Y. Yamamoto, C. Ito, R. Yoshida, S. Suzuki, N. Sasaki, M. Shibayama, U.I. Chung, Design and fabrication of a high-strength hydrogel with ideally homogeneous network structure from tetrahedron-like macromonomers, Macromolecules 41 (14) (2008) 5379–5384.

[57] S.Y. Fu, X.Q. Feng, B. Lauke, Y.W. Mai, Effects of particle size, particle/matrix interface adhesion and particle loading on mechanical properties of particulate–polymer composites, Compos. B Eng. 39 (6) (2008) 933–961.

[58] J.D. Hood, F. Ricardo, W.B. Kiosses, M.A. Schwartz, D.A. Cheresh, Differential alphav integrin-mediated Ras-ERK signaling during two pathways of angiogenesis, JCB (J. Cell Biol.) 162 (5) (2003) 933–943.

[59] G.T.A. Salazar, Review of biophysical factors affecting osteogenic differentiation of human adult adipose-derived stem cells, Biophysical Reviews 5 (1) (2013) 11–28.

[60] Y. Liang, J. Li, Q. Lin, P. Huang, L. Zhang, W. Wu, Y. Ma, Research progress on signaling pathway-associated oxidative stress in endothelial cells, Oxidative Medicine and Cellular Longevity,2017,(2017-4-19) 2017 (28) (2017) 1–8.

[61] G.N. Masoud, W. Li, HIF-1 α pathway: role, regulation and intervention for cancer therapy, Acta Pharm. Sin. B 5 (5) (2015) 378–389.

[62] N. Hohmann, N. Xia, K. Steinkamp-Fenske, U. Fã¶Rstermann, H. Li, Estrogen receptor signaling and the PI3K/Akt pathway are involved in Betulinic acid-induced eNOS activation, Molecules 21 (8) (2016) 973.

[63] M. Zhu, J. Li, K. Wang, X. Hao, R. Ge, Q. Li, Isoquercitrin inhibits hydrogen peroxide-induced apoptosis of EA.hy926 cells via the PI3K/Akt/GSK3î² signaling pathway, Molecules 21 (3) (2016) 356.

[64] M. Daniel, L. Yi, Y. Junyao, W. Gang, M. Andriana, J. Zhixin, Y. Hui, Z. Anna, H. Yanhua, X. Qingbo, Unspliced X-box-binding protein 1 (XBP1) protects endothelial cells from oxidative stress through interaction with histone deacetylase 3, J. Biol. Chem. 289 (44) (2014) 30625–30634.

[65] W. Luo, S.R. Jones, M.N. Yousaf, Geometric control of stem cell differentiation rate on surfaces, Langmuir the Acs Journal of Surfaces & Colloids 24 (21) (2008) 12129.

[66] K.A. Kilian, B. Bugarija, B.T. Lahn, M. Mrksich, Geometric cues for directing the differentiation of mesenchymal stem cells, Proc. Natl. Acad. Sci. U. S. A. 107 (11) (2010) 4872–4877.

[67] However, C. specifically, Contacts, forces, external, controlling self-renewal and differentiation of stem cells via mechanical cues, J. Biomed. Biotechnol. 2012 (3) (2012) 797410.

[68] A.J. Engler, S. Sen, H.L. Sweeney, D.E. Discher, Matrix elasticity directs stem cell lineage specification, Cell 126 (4) (2006) 677.

[69] B.P. Kanungo, L.J. Gibson, Density-property relationships in collagen-glycosaminoglycan scaffolds, Acta Biomater. 6 (2) (2010) 344–353.

[70] F.M. Chen, J. Zhang, M. Zhang, Y. An, F. Chen, Z.F. Wu, A review on endogenous regenerative technology in periodontal regenerative medicine, Biomaterials 31 (31) (2010) 7892–7927.

[71] A. Mehrkens, F. Saxer, S. Güven, W. Hoffmann, A.M. Müller, M. Jakob, F.E. Weber, I. Martin, A. Scherberich, Intraoperative engineering of osteogenic grafts combining freshly harvested, human adipose-derived cells and physiological doses of bone morphogenetic protein-2, Eur. Cell. Mater. 24 (7) (2012) 308–319.

[72] A.B. Rabie, R.W. Wong, U. Hagg, Composite autogenous bone and demineralized bone matrices used to repair defects in the parietal bone of rabbits, Br. J. Oral Maxillofac. Surg. 38 (5) (2000) 565–570.

[73] P.H. Cha, W. Shin, M. Zahoor, H.Y. Kim, D.S. Min, K.Y. Choi, Hovenia dulcis Thunb extract and its ingredient methyl vanillate activate wnt/β-catenin pathway and increase bone mass in growing or ovariectomized mice, PloS One 9 (1) (2014), e85546.

[74] T.K. Hyun, S.H. Eom, C.Y. Yu, T. Roitsch, Hovenia dulcis–an Asian traditional herb, Planta Med. 76 (10) (2010) 943–949.

[75] P. Kloen, M.C. Gebhardt, A. Perez-Atayde, A.E. Rosenberg, D.S. Springfield, L. I. Gold, H.J. Mankin, Expression of transforming growth factor-beta (TGF-beta) isoforms in osteosarcomas: TGF-beta3 is related to disease progression, Cancer 80 (12) (1997) 2230–2239.

[76] J. Massague, S.W. Blain, R.S. Lo, TGFbeta signaling in growth control, cancer, and heritable disorders, Cell 103 (2) (2000) 295–309.

[77] X. Luo, J. Chen, W.X. Song, N. Tang, J. Luo, Z.L. Deng, K.A. Sharff, G. He, Y. Bi, B. C. He, E. Bennett, J. Huang, Q. Kang, W. Jiang, Y. Su, G.H. Zhu, H. Yin, Y. He, Y. Wang, J.S. Souris, L. Chen, G.W. Zuo, A.G. Montag, R.R. Reid, R.C. Haydon, H. H. Luu, T.C. He, Osteogenic BMPs promote tumor growth of human osteosarcomas that harbor differentiation defects, Laboratory investigation; a journal of technical methods and pathology 88 (12) (2008) 1264–1277.

[78] K. Kn, O. B, S. Hc, P.h. Rk, A. Ia, C. R, Raman spectra of graphite oxide and functionalized graphene sheets, Nano Lett. 8 (1) (2007) 36.

[79] X. Sun, Z. Liu, K. Welsher, J.T. Robinson, A. Goodwin, S. Zaric, H. Dai, Nano-graphene oxide for cellular imaging and drug delivery, Nano research 1 (3) (2008) 203–212.